Canonical IRE1 function needed to sustain vigorous natural killer cell proliferation during viral infection

Jessica Vetters, Mary van Helden, Clint de Nolf, Sofie Rennen, Eva Cloots, Evelien van de Velde, Farzaneh Fayazpour, Justine van Moorleghem, Manon Vanheerswynghels, Karl Vergote, et al.

▶ To cite this version:

Jessica Vetters, Mary van Helden, Clint de Nolf, Sofie Rennen, Eva Cloots, et al.. Canonical IRE1 function needed to sustain vigorous natural killer cell proliferation during viral infection. iScience, 2023, 26 (12), pp.108570. ⟨10.1016/j.isci.2023.108570⟩. ⟨hal-04542884⟩

HAL Id: hal-04542884
https://amu.hal.science/hal-04542884v1

Submitted on 11 Apr 2024

iScience

CellPress OPEN ACCESS

Article

Canonical IRE1 function needed to sustain vigorous natural killer cell proliferation during viral infection

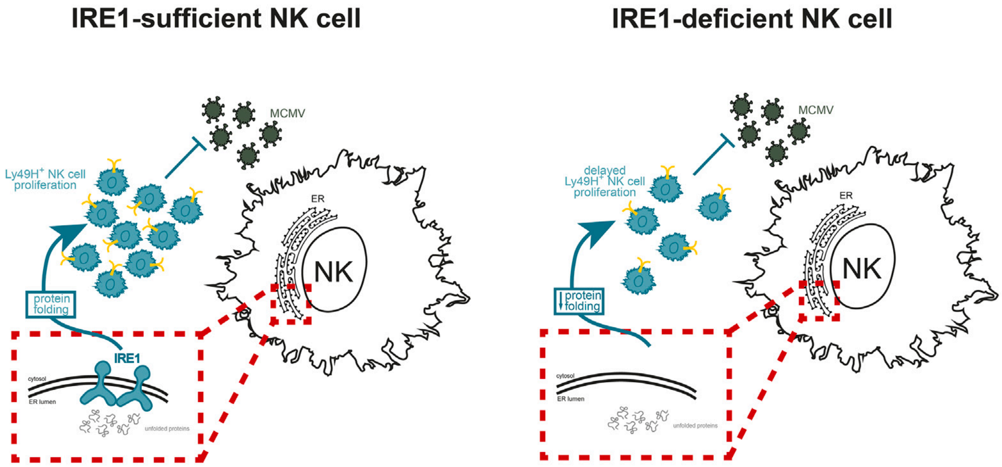

Jessica Vetters, Mary van Helden, Clint De Nolf, ..., Eric Vivier, Bart N. Lambrecht, Sophie Janssens

sophie.janssens@irc.vib-ugent.be

Highlights

IRE1 is dispensable for steady state NK cell homeostasis

IRE1 deficiency impairs NK cell proliferation during MCMV infection

This is due to major defects in IRE1's canonical function in protein homeostasis

Yet, this does not affect the overall viral response of IRE1-deficient NK cells

Vetters et al., iScience *26*, 108570
December 15, 2023 © 2023 The Author(s).
https://doi.org/10.1016/j.isci.2023.108570

iScience

CellPress
OPEN ACCESS

Article

Canonical IRE1 function needed to sustain vigorous natural killer cell proliferation during viral infection

Jessica Vetters,[1,2] Mary van Helden,[2,3,4] Clint De Nolf,[1,2,5,6] Sofie Rennen,[1,2] Eva Cloots,[1,2] Evelien Van De Velde,[1,2] Farzaneh Fayazpour,[1,2] Justine Van Moorleghem,[2,3] Manon Vanheerswynghels,[2,3] Karl Vergote,[2,3] Louis Boon,[7] Eric Vivier,[8,9,10] Bart N. Lambrecht,[2,3,11] and Sophie Janssens[1,2,12,*]

SUMMARY

The unfolded protein response (UPR) aims to restore ER homeostasis under conditions of high protein folding load, a function primarily serving secretory cells. Additional, non-canonical UPR functions have recently been unraveled in immune cells. We addressed the function of the inositol-requiring enzyme 1 (IRE1) signaling branch of the UPR in NK cells in homeostasis and microbial challenge. Cell-intrinsic compound deficiency of IRE1 and its downstream transcription factor XBP1 in NKp46^{+} NK cells, did not affect basal NK cell homeostasis, or overall outcome of viral MCMV infection. However, mixed bone marrow chimeras revealed a competitive advantage in the proliferation of IRE1-sufficient Ly49H^{+} NK cells after viral infection. CITE-Seq analysis confirmed strong induction of IRE1 early upon infection, concomitant with the activation of a canonical UPR signature. Therefore, we conclude that IRE1/XBP1 activation is required during vigorous NK cell proliferation early upon viral infection, as part of a canonical UPR response.

INTRODUCTION

Natural killer (NK) cells are the founding members of the innate lymphoid cell (ILC) family of immune cells.[1,2] With their cytotoxic effector function, they are seen as the innate counterparts of cytotoxic T cells.[3] Cytotoxicity combined with an inherent capacity to produce large amounts of macrophage activating cytokines like IFNγ makes NK cells important effector cells in the anti-tumoral and anti-viral immune response.[4] Their activity is balanced by a range of germline-encoded activating and inhibitory receptors that react to self or non-self and by cytokines released by damaged or infected tissues or activated immune cells.[4,5] In mice, this is portrayed in the murine model of cytomegalovirus (MCMV) infection where Ly49H-bearing NK cells are specifically activated by recognition of the m157 viral ligand expressed on the surface of virus-infected cells.[6,7] Clonal-like expansion of this specific NK cell subset is required to confer host protection. Within a few days, the Ly49H^{+} NK cell population can expand up to 100- or 1000-fold in the spleen and liver of MCMV-infected mice,[8,9] highlighting the necessity for a well-equipped protein translational machinery that would allow rapid expansion of these cells under stress.

Among cellular organelles, the endoplasmic reticulum (ER) forms a central hub for protein synthesis. Whenever the ER's demand exceeds its folding capacity, improperly folded proteins will accumulate in the ER lumen. This leads to activation of the unfolded protein response (UPR), an adaptive cellular program to help restore ER homeostasis. Upon ER stress, three ER-resident sensors, inositol-requiring enzyme 1 (IRE1), protein kinase R-like ER kinase (PERK) and activating transcription factor 6 (ATF6), become activated and, each in their unique way, help re-establish ER homeostasis. When ER stress cannot be resolved, the UPR switches from its protective mode toward a destructive mode, ultimately leading to the induction of programmed cell death.[10–12] The endonuclease IRE1 is the most conserved UPR sensor and its endonuclease domain mainly targets X-box binding protein 1 (XBP1) mRNA. Unconventional cleavage of XBP1-unspliced (XBP1-u) gives rise to XBP1-spliced (XBP1-s), that upon translocation to the nucleus acts as a potent transcription factor regulating genes involved in lipid

---

[1] Laboratory for ER Stress and Inflammation, VIB Center for Inflammation Research, Ghent, Belgium
[2] Department of Internal Medicine and Pediatrics, Ghent University, Ghent, Belgium
[3] Laboratory for Immunoregulation and Mucosal Immunology, VIB Center for Inflammation Research, Ghent, Belgium
[4] Byondis B.V., Nijmegen, the Netherlands
[5] Laboratory for Barriers in Inflammation, VIB Center for Inflammation Research, Ghent, Belgium
[6] Department of Biomedical Molecular Biology, Ghent University, Ghent, Belgium
[7] JJP Biologics, Warsaw, Poland
[8] Aix Marseille University, CNRS, INSERM, Centre d'Immunologie de Marseille-Luminy, Marseille, France
[9] AP-HM, Hôpital de la Timone, Marseille-Immunopôle, Marseille, France
[10] Innate Pharma Research Laboratories, Innate Pharma, Marseille, France
[11] Department of Pulmonary Medicine, Erasmus MC, Rotterdam, the Netherlands
[12] Lead contact
*Correspondence: sophie.janssens@irc.vib-ugent.be
https://doi.org/10.1016/j.isci.2023.108570

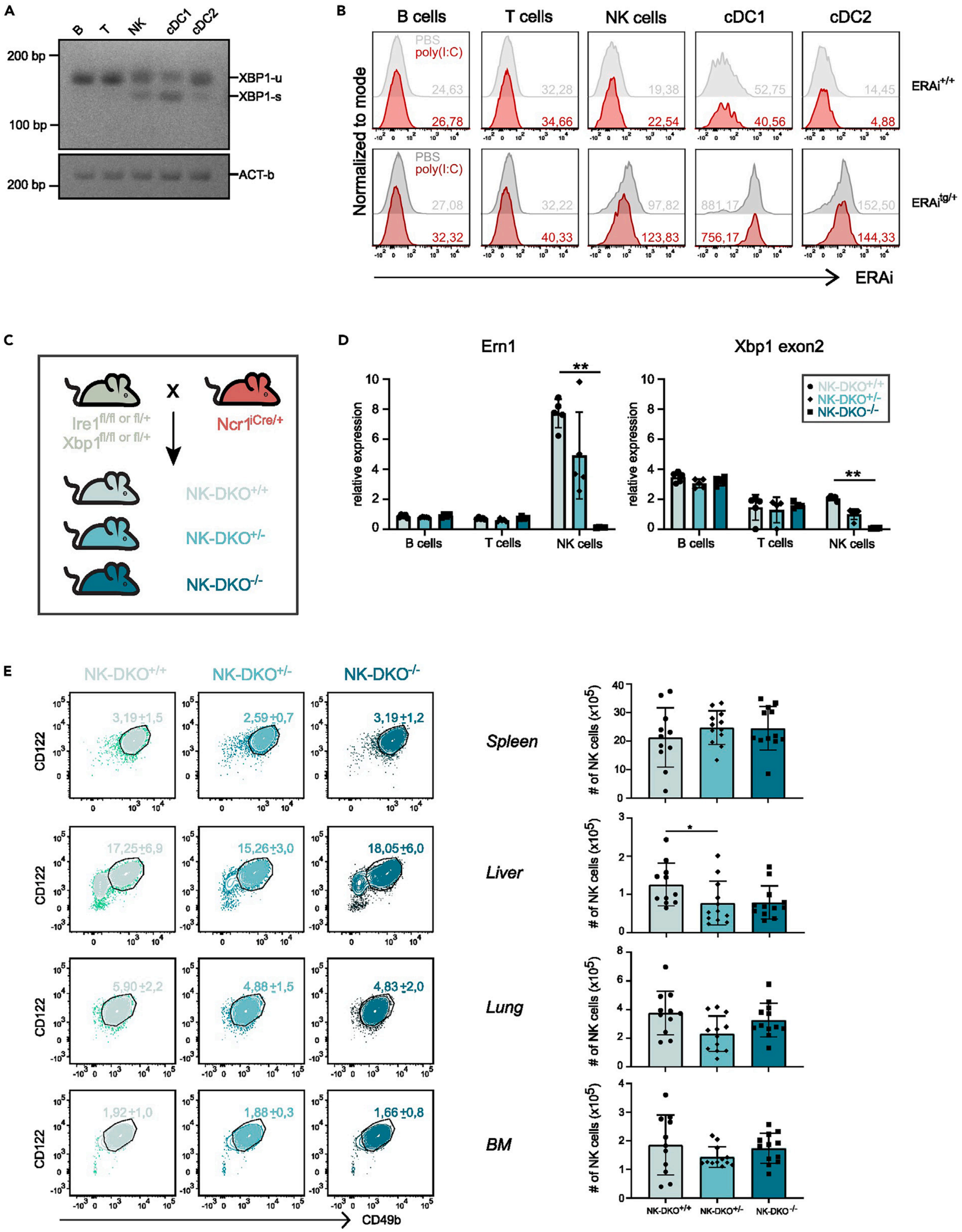

Figure 1. NK cell distribution remains unaltered upon loss of IRE1/XBP1

(A) Conventional PCR for both XBP1 isoforms (u, unspliced and s, spliced) on cDNA isolated from wild type sorted splenic immune cell populations. Actin-beta expression was used as reference.

Figure 1. *Continued*

(B) Flow cytometry analysis of ERAi signal as measured on immune cell populations isolated from the spleens of ERAi$^{+/+}$ (top panels) and ERAi$^{tg/+}$ (bottom panels) animals after 12 h treatment with PBS or 100 μg poly(I:C). Numbers on histograms depict the average ERAi mean fluorescence intensity (MFI) per cell type.
(C) Graphical representation of the NK-DKO mouse model.
(D) Mouse model validation by qPCR on RNA that was isolated from sorted splenic lymphocytes of NK-DKO$^{+/+}$, NK-DKO$^{+/-}$ and NK-DKO$^{-/-}$ animals. Bar graphs represent Ern1 and Xbp1 exon 2 expressions as normalized to Sdha and Ywhaz.
(E) NK cell distribution across organs of NK-DKO$^{+/+}$, NK-DKO$^{+/-}$ and NK-DKO$^{-/-}$ animals as measured by flow cytometry. Bar graphs depict absolute NK cell numbers and contour plots represent the average percentage of NK cells ±SD (within live, CD45^{+} gate). For all figures, data is representative of 1 (D) or 2 independent experiments (A, B) or contains data from 3 pooled independent experiments (E). Bar graphs represent mean ± SD and dots represent individual mice. See also Figure S1. Statistics: (B) Mann-Whitney U test for comparison of both treatments, (D and E) Kruskal-Wallis test with Dunn's test to correct for multiple comparisons. *p < 0.05; **p < 0.01; ***p < 0.001; ****p < 0.0001.

biosynthesis, ER expansion and ER-associated degradation.[13,14] Besides XBP1, IRE1's RNase domain also cleaves several other ER-located mRNAs in a process called regulated IRE1-dependent decay (RIDD).[15]

Based on the notion that some immune cell types show high steady state activation of ER stress signaling branches in the absence of a typical UPR signature, it has been postulated that the UPR has additional functions in immune cells, contributing to immune cell development, differentiation and function.[16,17] Along these lines, c-myc was identified as a novel target of the IRE1/XBP1 signaling branch in NK cells by bulk RNA sequencing (RNA-Seq). During viral infection, XBP1-dependent transcriptional activation of the *c-myc* gene was needed to support proliferation of activated NK cells and ensure NK cell-mediated anti-viral and anti-tumor immunity.[18] In addition, a recent study identified the proto-oncogene *Pim-2* as a transcriptional target gene of XBP1, needed to sustain NK cell survival in conditions of cytokine-activation.[19]

With high resolution technology such as single-cell RNA-Seq now widely available, it has become clear that some of the previously identified differentially expressed (DE) genes with bulk RNA-Seq are only reflecting the heterogeneity in cellular populations between different genotypes rather than representing genes that are truly affected by the absence or presence of certain key components (for an example see[20]). To address the role of IRE1 in NK cell biology, we therefore made use of a single cell sequencing approach - both in steady state and during viral infection - to assess which genes were regulated in an IRE1/XBP1-dependent manner over the course of a viral infection. This revealed that the majority of genes induced in response to MCMV, including *c-myc* and cell cycle genes, were not altered in absence of IRE1/XBP1 signaling in NK cells. While we could not corroborate the proposed role for IRE1 in driving *c-myc* expression, we did confirm the need for a properly functioning UPR to support rapid proliferation of virus-specific NK cells, in line with IRE1's canonical role in maintaining protein homeostasis.

RESULTS

NK cell distribution and function remain unaltered upon loss of IRE1 and/or XBP1

In most cell types, the IRE1 signaling axis is not active in basal conditions but reporter studies have shown that conventional dendritic cells (cDCs), macrophages and NK cells are exceptions to this rule.[21,22] Compared to splenic T and B cells, NK cells showed basal XBP1 splicing activity, as determined by conventional PCR on sorted splenic immune cell populations (Figure 1A) or by monitoring IRE1 endonuclease activity by means of the ER stress-activated indicator (ERAi) VenusFP reporter mouse line[23] (Figure 1B). Still, compared to type 1 cDCs (cDC1s), the endonuclease activity of IRE1 in NK cells appeared modest, even after stimulation of NK cells with the viral analog poly(I:C) (Figure 1B). To assess the role of IRE1 in NK cells, two genetically modified mouse lines were generated by crossing *Ncr1*$^{iCre/+}$ mice[24] to *Xbp1*$^{fl/fl}$[25] or *Ire1*$^{fl/fl}$ x *Xbp1*$^{fl/fl}$[26] animals. A schematic overview of the generation of both mouse lines is depicted in Figures S1A and S1C and the lines will be referred to as NK-XBP1-KO and NK-DKO. We chose to generate a double deficient IRE1/XBP1 knockout (DKO) to distinguish true XBP1 transcriptional effects from regulated IRE1-dependent decay (RIDD)-mediated effects. Indeed, we previously found that loss of XBP1 in cDC1s led to IRE1 hyperactivation and IRE1-dependent decay of specific mRNAs, known as RIDD.[21] Transcriptional target genes of XBP1 are expected to be downregulated in both mouse lines, while RIDD target genes will be downregulated in the XBP1 KO but restored in DKO NK cells.

Both lines were first validated by qPCR on sorted splenic immune cell populations, which showed deletion of *Xbp1* and/or *Ern1* (encoding for IRE1) in NK cells but not T or B cells, denoting the specificity of our targeting approach (Figures S1B and S1D). NK cell distribution, both in absolute numbers as well as percentages of live, CD45^{+} cells, remained largely unaltered by loss of *Xbp1* or *Ern1/Xbp1*, in all organs examined (Figures S1C and S1E; contour plots represent percentages and bar graphs depict absolute numbers). Moreover, NK cell maturation - a process characterized by the sequential up- and downregulation of CD27 and concomitant upregulation of CD11b[27–29] - occurred normally in all organs examined in both mouse lines (Figures S1D and S1E; percentages not shown).

Next, flow cytometric analysis of NK cell function revealed that loss of IRE1/XBP1 did not affect IFNγ production or degranulation (with the latter assessed by CD107a surface expression, a well-established marker for NK cell degranulation[30]) in either steady state or upon *ex vivo* cytokine stimulation (Figure 2A). Both functions were however slightly hampered upon plate-bound antibody restimulation against Ly49D (Figure 2A), which was most likely due to a decreased percentage of Ly49D-expressing NK cells in IRE1/XBP1-deficient animals (Figure 2B) rather than being a direct result of IRE1/XBP1 loss on NK cell function. Similar observations were made in NK-XBP1-KO animals (Figure S2A). Although previous research in macrophages showed IFNγ secretion to be regulated by IRE1-dependent activation of XBP1,[31] we did not observe any differences in IFNγ secretion between DKO$^{+/+}$ and DKO$^{-/-}$ NK cells (Figure 2C).

To gain more insight in the potential role of the IRE1/XBP1 signaling branch in steady state NK cells, bulk RNA-Seq was performed on total splenic NK cells sorted from NK-XBP1-KO$^{-/-}$, NK-DKO$^{-/-}$ and their respective littermates (Figure 2D; Table S1). *Xbp1* expression was clearly

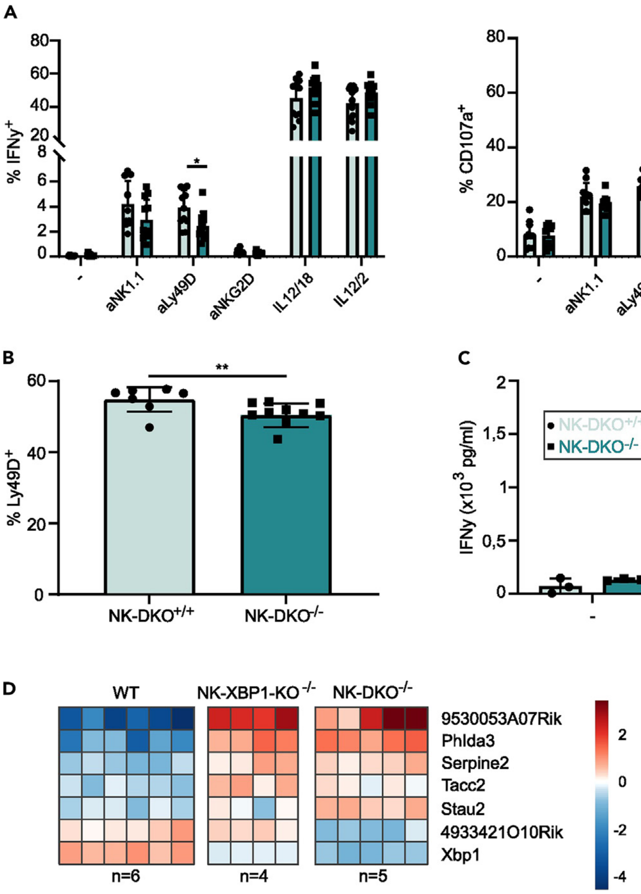

Figure 2. Limited role for IRE1/XBP1 in NK cell homeostasis and function

(A–C) Flow cytometry analysis of NK cells isolated from the spleens of NK-DKO$^{+/+}$ and NK-DKO$^{-/-}$ animals. (A) Bar graphs depict percentage IFNγ^{+} (left) or CD107a^{+} (right) NK cells as measured upon 4 h *ex vivo* culture with or without stimulation. (B) Bar graphs show percentage Ly49D^{+} NK cells among total splenic NK cells. (C) IFNγ ELISA on culture supernatant of sorted splenic NK cells cultured for 24 h in presence or absence of cytokine stimulation.

(D) Bulk RNA sequencing of steady state NK cells isolated from the spleens of NK-XBP1-KO and NK-DKO mouse lines. Heatmap contains all DE genes between XBP1-KO$^{-/-}$, DKO$^{-/-}$ and their respective littermate NK cells. The color scale indicates the scaled log2 normalized gene expression. Panels A-B display data from pooled experiments, panel C is representative of 3 independently conducted experiments and RNA-Seq (D) was performed a single time. Bar graphs plot the mean ± SD; for panel C the mean was calculated from 3 to 6 technical replicates per sample. Dots and heatmap squares represent individual mice. See also Figure S2 and Table S1. Statistics: Mann-Whitney U test (A–C) or see STAR Methods (D) for details. $^{*}p < 0.05$; $^{**}p < 0.01$; $^{***}p < 0.001$; $^{****}p < 0.0001$.

downregulated in both XBP1-KO$^{-/-}$ and DKO$^{-/-}$ NK cells, confirming the previously obtained qPCR results in our two mouse lines (Figures S1B; S1D). Only six other genes appeared differentially expressed between the three genotypes, underscoring the limited role of the IRE1/XBP1 signaling branch in steady state NK cells (Figure 2D; Table S1). Among these DE genes, the pleckstrin homology like domain family 1 member 3 (*Phlda3*) has previously been identified as an XBP1 target gene.[32,33] However, in our hands, the gene appeared upregulated - not downregulated - in the absence of XBP1. Also the serine protease inhibitor *Serpine 2*,[34] the RNA binding protein *Staufen 2*[35] and the centrosomal adaptor protein *Tacc2*[36] appeared upregulated in both XBP1-KO$^{-/-}$ and DKO$^{-/-}$ NK cells. Of note, we did not identify any genes that were specifically downregulated in XBP1-KO$^{-/-}$ NK cells and restored in DKO$^{-/-}$ NK cells, indicating that RIDD was not induced upon loss of XBP1 in NK cells, in contrast to what we noticed before for cDC1s.[21] This demonstrates again that activation of RIDD upon loss of *Xbp1* is specific to particular cell types only, and not a general consequence of the loss of XBP1.[21]

Taken together, NK cells do display weak basal IRE1 activity, but loss of IRE1 and/or XBP1 does not have any major impact on NK cell homeostasis or function in steady state conditions. This is supported by bulk RNA-Seq as hardly any DE genes were retrieved in the comparison of the transcriptomes of XBP1-KO$^{-/-}$ or DKO$^{-/-}$ NK cells to the transcriptome of littermate controls. As we did not observe any RIDD activity upon deletion of *Xbp1* in NK cells, we decided to focus on the NK-DKO mouse line for the remaining part of the story.

IRE1/XBP1 is required for NK cell proliferation upon viral infection

As NK cells play a prominent role in anti-viral immunity, especially against herpesviruses,[37,38] we next sought to determine if absence of IRE1/XBP1 would affect NK cell responses to murine cytomegalovirus (MCMV). In a first step, we assessed the overall response of NK-DKO$^{+/+}$ and

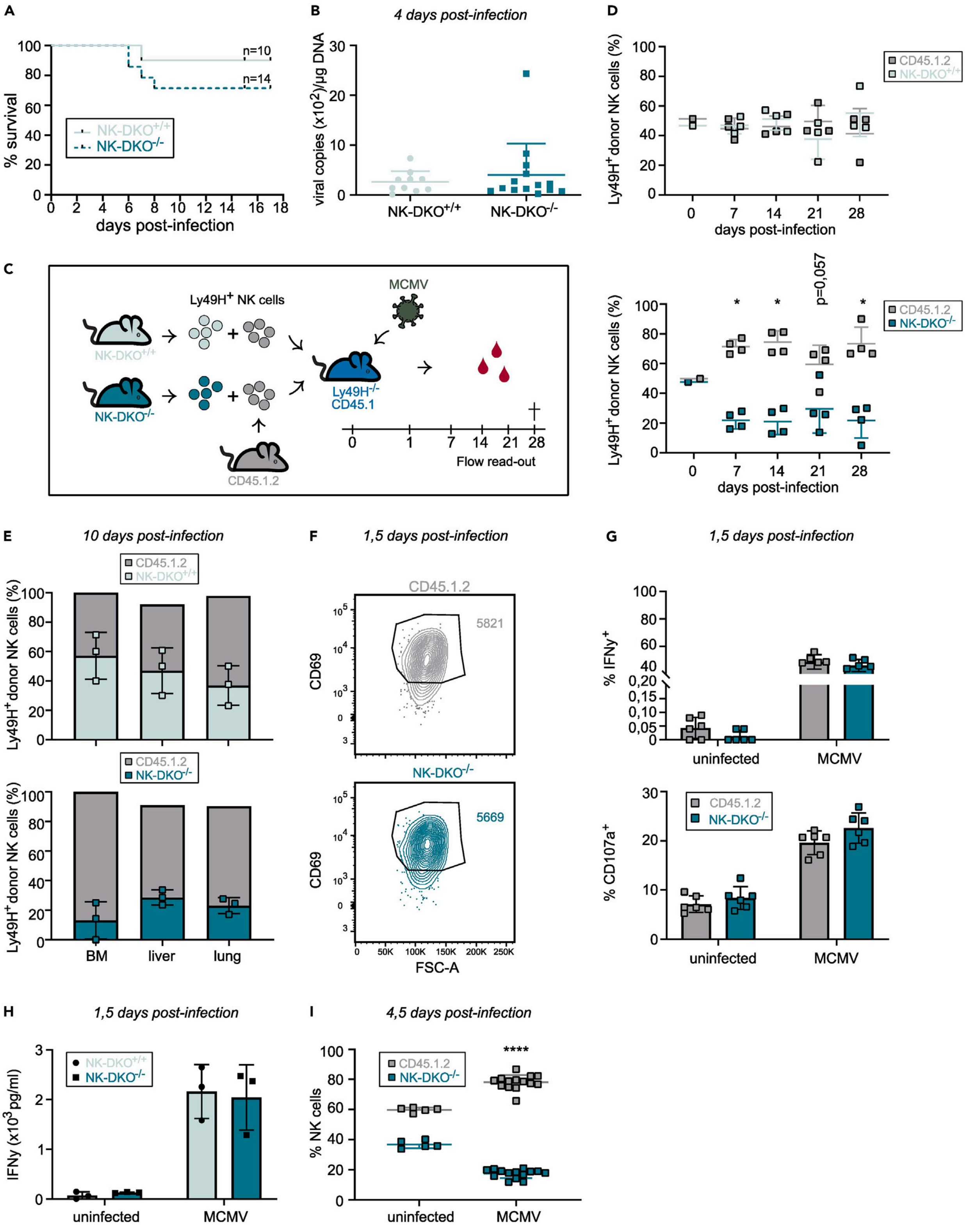

Figure 3. Loss of IRE1/XBP1 hampers NK cell expansion upon viral infection

(A and B) High dose MCMV infection of NK-DKO mice. (A) Kaplan-Meier curves display overall survival of infected animals. (B) Viral loads as determined by qPCR in the blood of infected animals 4 dpi.

Figure 3. ***Continued***

(C) Graphical representation of competitive cell transfer setups.

(D and E) Flow cytometry analysis of donor Ly49H^{+} NK cells after transfer into MCMV-infected Ly49H$^{-/-}$ hosts. (D) Percentage CD45.1.2 and CD45.2 (top: DKO$^{+/+}$, bottom: DKO$^{-/-}$) donor Ly49H^{+} NK cells in the blood at different time points post-infection. (E) Percentage CD45.1.2 and CD45.2 (top: DKO$^{+/+}$, bottom: DKO$^{-/-}$) donor Ly49H^{+} NK cells in indicated organs 10 dpi.

(F, G, I) Flow analysis of splenic NK cells isolated from DKO$^{-/-}$:CD45.1.2 mixed bone marrow chimeras infected with MCMV or mock treated. (F) Contour plots show average CD69 MFI of CD45.1.2 and CD45.2 (DKO$^{-/-}$) NK cells 1,5 dpi MCMV. (G) Bar graphs display percentage IFNγ^{+} (top) and CD107a^{+} (bottom) CD45.1.2 and DKO$^{-/-}$ NK cells 1,5 dpi mock or MCMV-infected.

(H) IFNγ ELISA on culture supernatant of sorted splenic NK cells from uninfected or 1,5 dpi MCMV-infected NK-DKO$^{+/+}$ or NK-DKO$^{-/-}$ animals. (I) Percentage donor NK cells retrieved in the spleens of mixed bone marrow chimeras 4,5 dpi mock or MCMV-infected. Data is representative for 1 out of 2 (D-G, I) or 3 (H) independent experiments or contains pooled data from 3 independent experiments (A-B). Bar graphs plot the mean ± SD; for panel H the mean was calculated from 3 to 6 technical replicates per sample. Dots represent individual mice. Lines in Kaplan-Meier curve (A) represent n = 10 or n = 14 for both respective groups. Statistics: Mantel-Cox test (A) or Mann-Whitney U test (B, D–I). $^{*}p < 0.05$; $^{**}p < 0.01$; $^{***}p < 0.001$; $^{****}p < 0.0001$.

NK-DKO$^{-/-}$ animals to a *mild* viral infection by infecting the mice with 2,5x10^{4} pfu/g MCMV (Figures S2B–S2E). A modest but clear reduction in initial bodyweight occurred during the first day post-infection (dpi), irrespective of the genotype (Figure S2B). Also, the initial viral control by NK cells, as determined by surface expression of the activation marker CD69 (Figure S2C) and early inflammatory cytokine-driven IFNγ production (Figure S2D) at 1,5 dpi appeared unaffected in conditions of IRE1/XBP1-deficiency (Figures S2C and S2D). On the contrary, we noted a modest but significant reduction in the percentage of Ly49H^{+} NK cells in NK-DKO$^{-/-}$ animals at the peak of infection (7 dpi) (Figure S2E). Considering Ly49H is the activating NK cell receptor providing resistance to MCMV by recognizing the m157 viral epitope on the surface of infected cells,[6,7] these data indicate that loss of IRE1/XBP1 might affect the proliferation of virus-specific NK cells during *mild* viral infection, without hampering any of the early steps in viral control.

To investigate this further, we challenged the mice with a *high* dose of MCMV corresponding to 5x10^{4} pfu/g. When assessing overall susceptibility to MCMV infection, NK-DKO$^{-/-}$ animals appeared slightly more susceptible than their littermates, but the observed differences were not statistically significant (Figure 3A). Moreover, when comparing viral loads at 4 dpi in the blood of infected animals we found no statistical differences between the two genotypes (Figure 3B). Next, competitive cell transfers were set up according to the graphical representation in Figure 3C. In brief, equal numbers of Ly49H^{+} NK cells were sorted from the spleens of NK-DKO$^{+/+}$, NK-DKO$^{-/-}$ and CD45.1.2 animals and 50:50 cell mixtures of CD45.1.2 and NK-DKO$^{+/+}$ or NK-DKO$^{-/-}$ were administered intravenously (iv) into CD45.1 Ly49H-deficient hosts. One day later, the hosts were challenged with MCMV with a dose that was lowered to 7,5x10^{3} pfu/g to account for their increased genetically predetermined susceptibility to the virus.[39] Donor Ly49H^{+} NK cell responses were assessed in the blood by flow cytometry at 7, 14, 21 and 28 dpi. For the DKO$^{+/+}$:CD45.1.2 cell mixture (Figure 3D, top), i.e., representing the wild type (WT) situation, donor percentages maintained 50:50 throughout the entire experiment. This ratio however drastically shifted toward the CD45.1.2 WT cells after administering the DKO$^{-/-}$:CD45.1.2 cell mixture at all time points examined (Figure 3D, bottom). The difference in ratio could not be explained by trafficking defects as donor percentages in different organs mirrored the situation in the blood (Figure 3E).

To tease out potential differences in early viral control, we generated DKO$^{-/-}$:CD45.1.2 mixed bone marrow chimeras (BMC). Therefore, CD45.1 acceptors were sublethally irradiated and replenished with a 50:50 mixture of hematopoietic progenitor cells isolated from the bone marrow of NK-DKO$^{-/-}$ and CD45.1.2 animals. At least 8 weeks after reconstitution, when donor chimerism was established, CD45.1 hosts were infected with MCMV and NK cell activation and function was assessed 1,5 days later. Both the percentage of CD69-expressing NK cells (data not shown) as well as CD69 expression on a per cell basis were comparable for splenic NK cells from DKO$^{-/-}$ and CD45.1.2 origin (Figure 3F). Also NK cell function, IFNγ production and degranulation, monitored on *ex vivo* cultured splenocytes isolated from the same DKO$^{-/-}$:CD45.1.2 BMCs, revealed no difference between IRE1/XBP1-deficient NK cells and their WT CD45.1.2 counterparts (Figure 3G). With IRE1 being a key sensor of the UPR, we wanted to exclude any potential posttranscriptional defects on IFNγ folding and secretion, but did not observe any differences in IFNγ levels in the supernatant of *ex vivo* cultured NK cells sorted from the spleens of NK-DKO$^{+/+}$ and NK-DKO$^{-/-}$ animals 1,5 days after infection with MCMV (Figure 3H). Despite the similarities in the degree of NK cell activation, loss of IRE1/XBP1 strongly decreased the percentage of DKO$^{-/-}$ NK cells isolated from the spleens of DKO$^{-/-}$:CD45.1.2 BMC as early as 4,5 dpi MCMV (Figure 3I). These data suggest a role for IRE1/XBP1 in the expansion of virus-specific NK cells, without affecting NK cell activation or initial viral control.

CITE-Seq analysis reveals heterogeneity in NK cell responses to MCMV infection

To address in more detail how loss of IRE1/XBP1 affects the NK cell response to viral infection, we used cellular indexing of transcriptomes and epitopes by sequencing (CITE-Seq), a method in which transcriptional information at single cell level is combined with expression of more than 150 different surface epitopes[40] (Table S2). To this end, we infected DKO$^{-/-}$:CD45.1.2 bone marrow chimeras with MCMV. At days 0 (i.e., uninfected controls), 1,5 and 4,5 post-infection, equal numbers of CD45.1.2 WT and CD45.2 DKO$^{-/-}$ splenic NK cells (gated as CD3^{-}CD19^{-}TCRβ^{-}NK1.1^{+}CD49b^{+}) were sorted. Lymphocytes (gated as non-NK) were spiked in to obtain a 50:50 ratio of NK cells to non-NK cells. Next, CD45.1.2 WT and CD45.2 DKO$^{-/-}$ sorted cells were processed separately for analysis by CITE-Seq.

We first analyzed the transcriptional changes that occurred in wild type NK cells upon challenge with MCMV. Sorted WT cells were obtained from each of the three time points (days 0, 1,5 and 4,5 post-infection) and merged into one large WT data object (Figure 4A). Unsupervised clustering and UMAP dimensionality reduction on the NK cell subset within this object (containing a total of 17664 NK cells) revealed

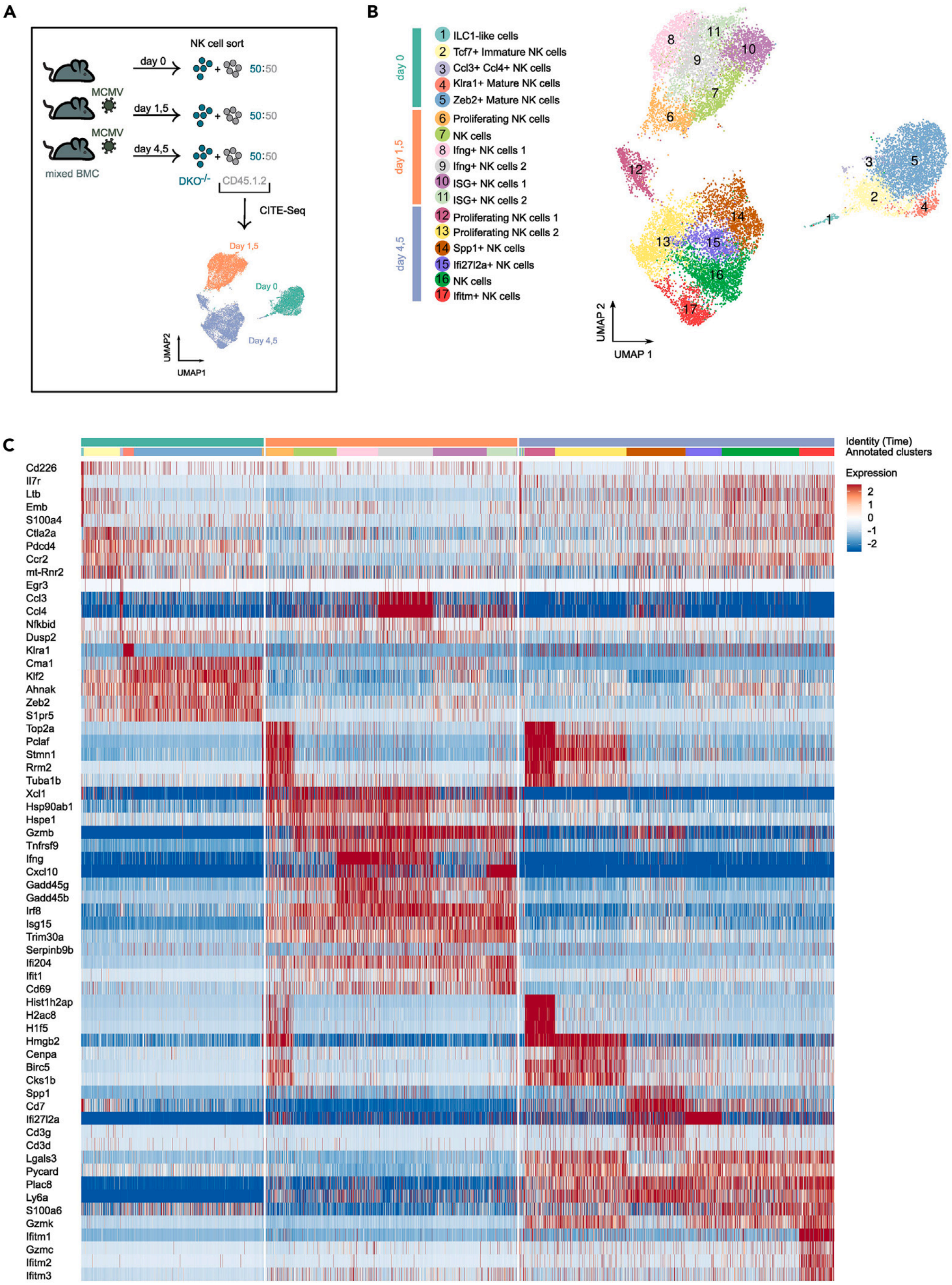

Figure 4. Transcriptional profiles of wild type (WT) NK cells upon MCMV infection

(A) Graphical representation of the CITE-Seq experimental setup to obtain a wild type (CD45.1.2) object. The scheme includes a simplified UMAP plot of all NK cells annotated according to the time variable (days 0, 1,5 and 4,5, respectively).

(B) Annotated UMAP of all NK cells collected from the WT object.

(C) Heatmap showing the normalized expression of the top 5 defining genes for each NK cell cluster in the WT object. The color bars at the top indicate both the time point and NK cell cluster annotation as indicated in (B). The color scale represents the normalized gene expression. See also Figures S3 and S4 and Tables S2, S3, S4, and S5. See STAR Methods for details on statistical testing.

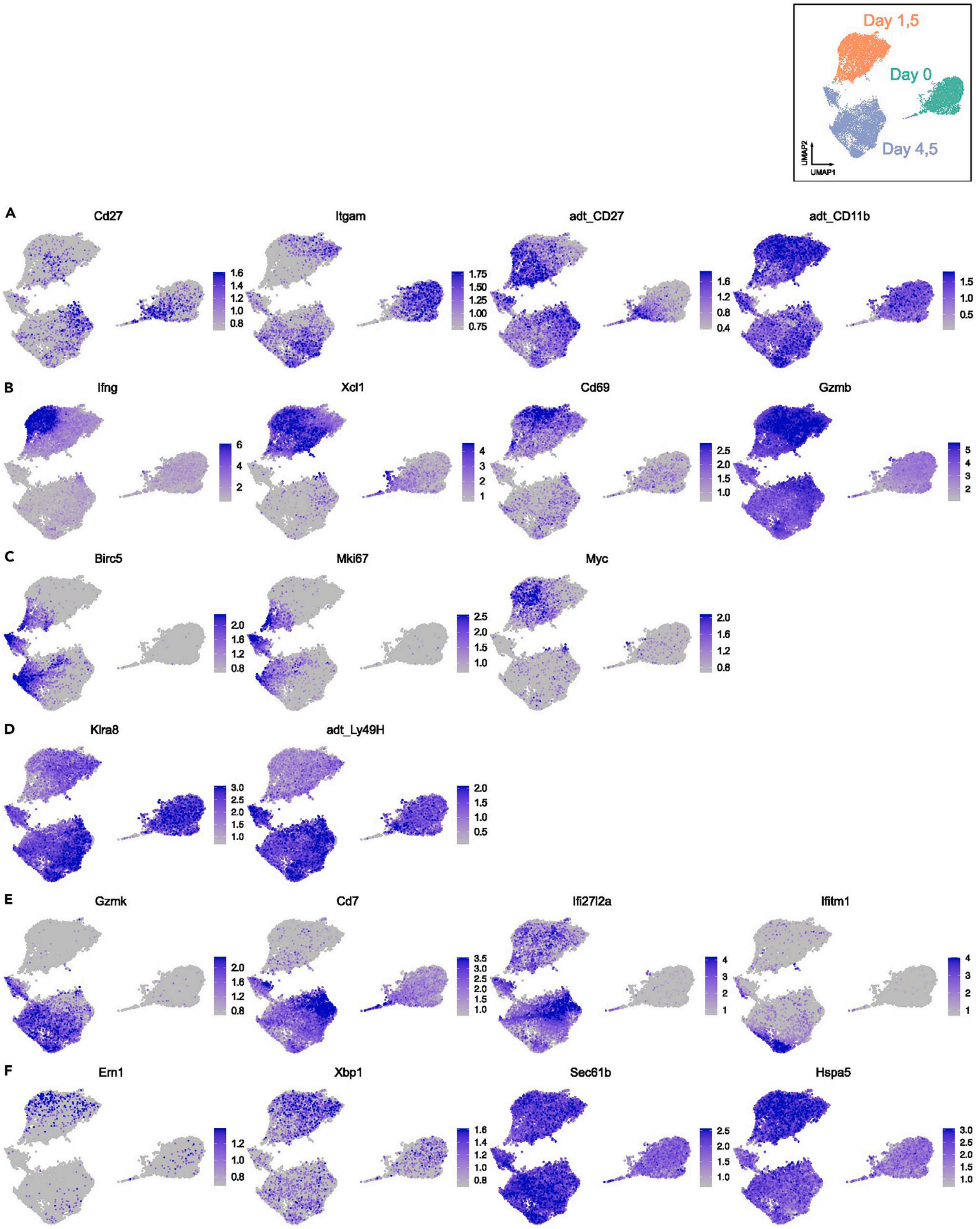
Day 1,5
Day 0
Day 4,5
UMAP2
UMAP1
A
Cd27
1.6 1.4 1.2 1.0 0.8
Itgam
1.75 1.50 1.25 1.00 0.75
adt_CD27
1.6 1.2 0.8 0.4
adt_CD11b
1.5 1.0 0.5
B
Ifng
6 4 2
Xcl1
4 3 2 1
Cd69
2.5 2.0 1.5 1.0
Gzmb
5 4 3 2
C
Birc5
2.0 1.6 1.2 0.8
Mki67
2.5 2.0 1.5 1.0
Myc
2.0 1.6 1.2 0.8
D
Klra8
3.0 2.5 2.0 1.5 1.0
adt_Ly49H
2.0 1.5 1.0 0.5
E
Gzmk
2.0 1.6 1.2 0.8
Cd7
3.5 3.0 2.5 2.0 1.5 1.0
Ifi27l2a
4 3 2 1
Ifitm1
4 3 2 1
F
Ern1
1.2 1.0 0.8
Xbp1
1.6 1.4 1.2 1.0 0.8
Sec61b
2.5 2.0 1.5 1.0
Hspa5
3.0 2.5 2.0 1.5 1.0

Figure 5. Visual representation of the transcriptional and surface epitope profiles of WT NK cells upon MCMV infection

(A–E) UMAP feature plots showing the expression of (A) maturation markers, (B) early effector genes, (C) proliferation genes, (D) *Klra8* with its surface protein counterpart Ly49H, (E) late effector genes and (F) UPR genes in wild type NK cells at days 0, 1,5 and 4,5 during MCMV infection. The cells on the plot are ordered according to expression, resulting in cells with high expression being plotted on top. The color scale represents normalized gene and surface expression. See also Figures S3 and S4 and Tables S2–S5

a primary clustering based on time point (Figure 4A). Further subclusters were annotated based on the expression of data-driven marker genes (Figure 4B; Table S3). The top 5 differentially expressed genes (DEGs) for each cluster were used to generate a heatmap (Figure 4C). Feature plots showing expression of specific genes or epitopes can be found in Figure 5. In uninfected, steady state conditions (day 0) five different clusters could be distinguished. Cluster 1 consisted of a very small group of cells that were *Il7r*$^{+}$*Sell*$^{-}$*Eomes*$^{-}$*Cd160*$^{+}$ (Figure S3A). Recently, a CD160^{+}CD62L^{-} (Figures S3A and S3B) population of "ILC1-like NK cells" has been described in the spleen that further expands upon MCMV infection.[41] However, these cells are *Eomes*$^{+}$*Batf3*$^{+}$*Id3*$^{+}$ and therefore do not appear to correspond to cluster 1 (Figure S3A). Based on detailed expression analysis of NK cell (*Eomes*) and ILC1 signature genes (*Rora*, *Il7r*, *Cxcr6*, *Cd200r1*, *Ikzf2*, *Zfp683*) cluster 1 appears to be a small population of ILC1-like cells that ended up in the NK1.1^{+}CD49b^{+} NK cell gate but are Hobit^{-} (encoded by *Zfp683*) (Figure S3A). This illustrates again the somewhat blurred borders between ILC1s and NK cells.[41–43] In line with earlier literature data,[41–43] NK cells could be easily separated into immature (cluster 2) or mature (clusters 4 and 5) subsets. Immature NK cells are CD27^{+}CD11b^{-} (Figure 5A)[27] and hallmarked by expression of *Tcf7*, *Cd226*, *Emb* and *Ctla2a* (cluster 2, Figure 4C). Mature NK cells are CD11b^{+}CD27^{-}KLRG1^{+} (Figure 5A; Figure S3B) and hallmarked by expression of *Klra1*, *Klf2*, *Cma1*, *Ahnak*, *S1pr5* or *Zeb2* (Figure 4C, clusters 4 and 5), genes needed amongst others for NK cell egress and terminal differentiation.[44] Within the mature NK cells, a very small group of cells (cluster 4) appears *Klra1*$^{+}$, however, the majority is *Klra1*$^{-}$ (cluster 5), with *Klra1* being a gene encoding the inhibitory receptor Ly49A. This highlights the known heterogeneity in Ly49 expression within the NK cell population.[45] Finally, we confirmed the presence of an inflammatory *Ccl3*$^{+}$*Ccl4*$^{+}$ chemokine producing subset (cluster 3) that has been identified before as a splenic-specific population of highly activated NK cells.[42]

MCMV infection led to massive changes on surface protein and transcriptional level of NK cells (Tables S3, S4, and S5). Upregulated Seurat marker genes for the total WT NK cell population between 1,5 dpi and day 0 were hallmarked by GO terms such as "regulation of defense response", "response to virus" and "positive regulation of cytokine production", while between 4,5 dpi and 1,5 dpi GO terms mainly referred to processes such as "actin cytoskeleton organization", "T cell activation" and "regulation of cell adhesion" (Table S5; Figure S4). At day 1,5 several well-established virus-induced transcriptional profiles were retrieved associated with early NK cell activation (*Cd69*), NK cell effector function (*Xcl1*, *Gzmb*, *Ifng*, …), induction of a type I IFN response (*Ifi204*, *Isg15*, *Zbp1*, …), chemokine expression (*Ccl3*, *Ccl4*, *Cxcl10* …), growth and apoptosis (*Gadd45 b/g*) or cell cycle and proliferation (*Pim*, *Myc*, *Irf8* (needed to control NK cell proliferation in response to MCMV[46]) (Table S5; Figure 4C; Figures 5B and 5C). A recent RNA-Seq study observed prominent transcriptional differences between Ly49H^{lo} and Ly49H^{hi} NK cells sorted early (d1,5) upon infection, showing a clear functional difference in the two subsets.[6] We noted that overall, both gene expression levels of *Klra8* and surface expression levels of Ly49H transiently declined at 1,5 dpi to rise massively at 4,5 dpi (Figure 5D). While *Klra8* did not turn out as a discriminating gene between different NK cell clusters within one timepoint - neither in uninfected conditions, nor at 1,5 or 4,5 dpi (Figure 5D) - we did note an inverse correlation between the expression of *Ifng* and cell surface expression of Ly49H (Figures 5B and 5D), corroborating earlier findings that especially Ly49H^{lo} cells are specialized in cytokine production.[6] Indeed, different NK cell clusters appear associated with different functional responses (Tables S3 and S4). At 1,5 dpi cluster 6 was marked by a proliferative gene signature (marked by genes such as *Top2a*, *Pclaf*, *Stmn1*, *Rrm2*, *Tuba1*), cluster 8 and 9 by expression of *Ifng* (respectively in absence (cluster 8) or presence (cluster 9) of chemokines *Ccl3/Ccl4),* while clusters 10 and 11 were marked by a strong type I interferon-stimulated genes (ISG) response, with cluster 11 additionally expressing *Cxcl10/Gbp5*. This reveals that not all genes previously associated with a viral transcriptional signature[47] are expressed in one and the same NK cell, supporting the concept of functional heterogeneity in NK cells.[6] From day 1,5 to day 4,5 p.i. we observed a marked shift in gene expression profile (Figure S4B; Table S5). Most chemokines were downregulated, just like early effector genes such as *Cd69*, *Ifng* or *Gzmb*, and many ISGs (Table S5). On the contrary, genes associated with T cell activation (such as *Cd7*, *Cd3g*), cytotoxic activity (*Gzmk*, *Gzmc*) or cytoskeletal rearrangements (*Vim*, *Coro1a*) were induced (Figure 5E). For other genes marking the 4,5 dpi core signature (Figure 4C), their function in NK cell biology is less established (*Lgals3*, *Pycard*, *Plac8* and *S100a6*).[48] More detailed analysis of the different subclusters at d4,5 revealed the presence of two proliferation clusters, with cluster 12 bearing a transcriptome profile highly similar to cluster 6 at day 1,5 and with cluster 13 expressing *Hmgb2*, *Cenpa*, *Birc5* and *Cks1b*, likely defining distinct stages within the cell cycle. Cluster 14 appears quite distinct from all other clusters at d4,5. It consists of more immature *Cd27*$^{+}$*Itgam*$^{-}$ NK cells (Figure 5A) that show markedly lower expression of cytotoxic molecules and *Pycard/Lgals3*, but high expression of molecules involved in communication with T cells (*Cd7*), as well as the osteopontin encoding gene *Spp1*.[49] Of note, this cluster is CD160^{+}CD62L^{-} (Figure S3B), hence might correspond to the cluster recently identified by Flommersfeld et al. that is essential for efficient communication with cDC1s and T cells upon MCMV infection.[41] Other clusters harbor expression of an anti-viral gene signature with a predominant expression of *Ifi27l2a* (cluster 15)[50] or *Ifitm* genes (cluster 16),[51] combined with expression of cytotoxic *Gzmk/c* molecules (Figure 5E). All in all, CITE-Seq analysis of NK cells at different stages of an MCMV infection reveal that there is a clear division in labor between different NK cell subsets, likely allowing them to perform a multitude of functions during viral infection.

Canonical role for IRE1/XBP1 in MCMV-driven NK cell proliferation

As described earlier,[18] one of the GO signatures induced at d1,5 post-infection was "protein folding" (Figure S4A), characterized by expression of marker genes *Ern1*, *Xbp1*, *Sec61* or *Hspa5* (Figure 5F). The two other branches from the UPR, PERK and ATF6, were not activated (data

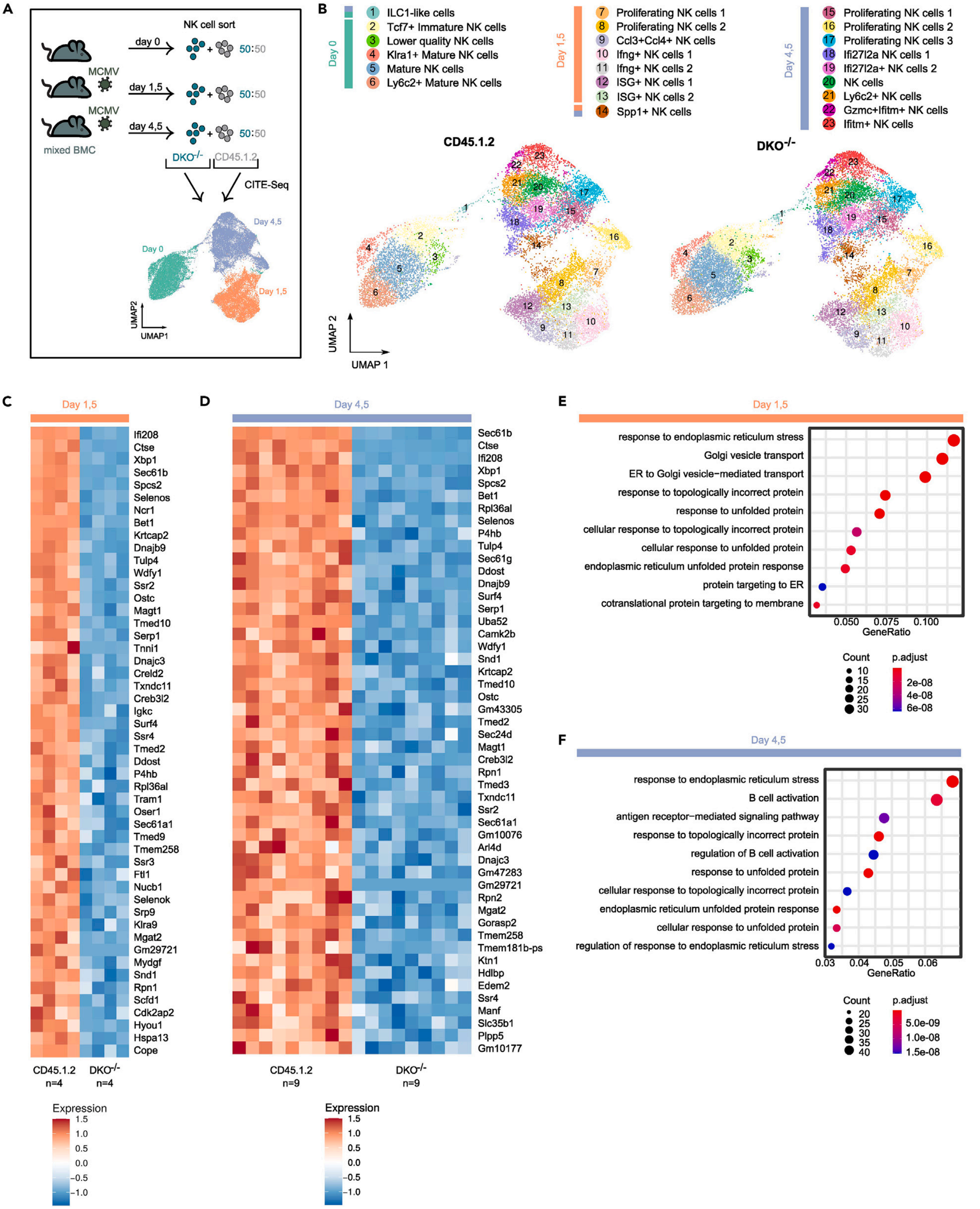

Figure 6. Canonical role for IRE1/XBP1 in MCMV-driven NK cell expansion

(A) Graphical representation of the CITE-Seq experimental setup to obtain one large object containing NK cells from WT (CD45.1.2) and DKO$^{-/-}$ (CD45.2) origin. The scheme includes a simplified UMAP plot of all WT and DKO$^{-/-}$ NK cells annotated according to the time variable (days 0, 1,5 and 4,5, respectively).

Figure 6. *Continued*

(B) Annotated UMAP of all NK cells collected from the combined WT/DKO$^{-/-}$ object.

(C and D) Cluster-sample pseudobulk heatmap of the muscat DS analysis for total NK cells between DKO$^{-/-}$ and WT at days 1,5 (n = 4) (C) or 4,5 (n = 9) (D) post-infection. The top 50 downregulated DE genes between DKO$^{-/-}$ and WT are shown. The color scale represents scaled mean logcounts.

(E and F) Dotplots featuring the top 10 significantly enriched biological pathway (BP) GO categories in the DE gene set between DKO$^{-/-}$ and WT NK cells at days 1,5 (E) or 4,5 (F) post-infection. These top GO categories are ordered according to the ratio of the input DE gene set annotated in the respective GO terms (geneRatio). The adjusted p value is displayed as the color of the dot and the size of the dot is determined by the number of DE genes annotated in the respective GO term (Count). See also Figure S5 and Tables S2, S6–S8 See STAR Methods for details on statistical testing.

not shown). To assess how loss of the IRE1/XBP1 axis affects the NK cell transcriptional response to viral infection and might interfere with NK cell expansion, we returned to the CITE-Seq experiment but this time directly merged sorted NK cells from CD45.1.2 WT and CD45.2 DKO$^{-/-}$ origin at all three time points (days 0, 1,5 and 4,5) into one large data object (Figures 6A and 6B, containing 37710 NK cells in total with 17664 WT and 20046 DKO$^{-/-}$ NK cells). Of note, since we knew from previous bone marrow chimera experiments (Figure 3I) that CD45.1.2 WT NK cells outcompete the CD45.2 DKO$^{-/-}$ NK cells (especially at 4,5 dpi MCMV), we decided to increase the number of animals at this specific time point to ensure collecting a sufficient number of CD45.2 DKO$^{-/-}$ NK cells for CITE-Seq. The number of sorted CD45.1.2 WT NK cells was adjusted to the number of CD45.2 DKO$^{-/-}$ NK cells to ensure a roughly equal sequencing depth for both genotypes, resulting in a fair comparison. Similar to the WT situation (Figures 4A and 4B), NK cells clustered together based on time point, and data-driven marker genes and surface proteins were used to further delineate different subclusters (Figures 6A and 6B; Tables S6 and S7). A thorough comparison of all subclusters revealed no differences in clusters of WT and DKO$^{-/-}$ origin (Figure 6B) and similar overall expression of key MCMV-induced transcripts such as *Ifng, Cd69* and *Xcl1* or *Gzmk, Birc5* and *Mki67* on days 1,5 and 4,5 post-infection, respectively (Figures S5A–S5D). Of note, *myc* was not picked up as one of the differentially expressed transcripts when comparing WT to DKO$^{-/-}$ NK cells (Table S8 and STAR Methods for applied cutoffs), in apparent contradiction to earlier findings.[18] In line with this, we did not detect any differences in *myc* mRNA expression when comparing WT and DKO$^{-/-}$ NK cells sorted 1,5 days after MCMV infection (Figure 7B). Similarly, neither the expression of myc target genes or any other cell cycle gene appeared affected (Figure S6A). Next, a heatmap was generated containing the top 50 significantly downregulated genes (see STAR Methods for applied cutoffs) between CD45.1.2 WT and CD45.2 DKO$^{-/-}$ NK cells at either 1,5 (Figure 6C) or 4,5 dpi (Figure 6D). By manual annotation, most of the top 50 downregulated genes in DKO$^{-/-}$ NK cells could be attributed to pathways such as the UPR (*Xbp1*, *Dnajb9*, *Creb3l2*, *Sec61b*, *Selenos*, *Ddost*), vesicular trafficking (*Bet1*, *Ssr2*, *SSr4*, *Tmed2*, *Tmed10*), post-translational modifications (*Tulp4*, *Tmem258*, *Krtcap2*, *Mgat2*, *P4hb*) or the overall immune response (*Ifi208*, *Ctse*, *Wdfy1*) (Table S8). A GO enrichment analysis on both DE gene sets (Table S8; Figures 6E and 6F for dotplot visualization on days 1,5 and 4,5, respectively) confirmed our manual annotation, highlighting the UPR as the most enriched GO category affected in the anti-viral response of DKO$^{-/-}$ NK cells. A selection of feature plots (Figure 7A) visualizes the downregulation of key transcripts assigned to the different manually annotated pathways, which was confirmed by qPCR analysis on sorted CD45.1.2 WT and CD45.2 DKO$^{-/-}$ NK cells at 1,5 dpi. (Figure 7B).

Taken together, these data reveal that loss of the IRE1/XBP1 axis does not affect any of the major viral responses induced by NK cells upon MCMV infection. On the contrary, cell-intrinsic loss of IRE1 in NK cells leads to a strongly impaired UPR at days 1,5 and 4,5 upon viral infection. We speculated that the absence of a fully operational folding machinery could affect the capacity of NK cells to deal with the increase in folding load during the virus-induced expansion phase, explaining the earlier observed difference in NK cell numbers in a competitive setting (Figure 3I). In line with this, we consistently observed a drop in Ki-67^{hi} CD45.2 DKO$^{-/-}$ cells compared to Ki67^{hi} CD45.1.2 WT cells in mixed bone marrow chimeras (Figure 7E), which was consistent throughout the whole kinetics of the experiment and accompanied by an increase in NK cells expressing intermediate levels of Ki-67 (Figure S6B). However, complementary approaches to monitor differences in cell proliferation such as the incorporation of 5-ethynyl-2′-deoxyuridine (EdU) (Figure S6C) or the use of membrane dilution dyes such as CellTrace Violet (CTV) (Figure S6D) did not reveal any gross difference between WT and DKO$^{-/-}$ NK cells. Also at gene expression level, we did not see any reduced expression of cell cycle genes (Table S8; Figure S6A), nor did we detect any difference in the estimated percentage of NK cells in the different phases of the cell cycle in the CITE-Seq experiment, as predicted by gene expression analysis[52] (Figures 7C and 7D). This corroborates earlier data obtained in Xbp1-deficient NK cells where, upon IL-15 stimulation and induction of ER stress, NK cell proliferation remained intact. Instead, Ma et al. discovered a XBP1-Pim-2 axis critical for NK cell survival,[19] an observation that we were unable to confirm in DKO$^{-/-}$ NK cells. Neither in steady state nor during infection, Pim-2 expression appeared affected due to loss of the IRE1/XBP1 branch (Figures S6E and S6F), coinciding with similar NK cell survival in both genotypes over the course of MCMV infection (Figure S6G). Therefore, we speculate that a small delay in early cellular NK cell expansion due to defects in folding might have large long-term ramifications in a competitive setting, leading to a preferential clonal expansion of the fitter WT cells. On the contrary, when comparing WT versus DKO$^{-/-}$ mice without competition, the effects of IRE1/XBP1 loss on NK cell expansion and viral control in the context of MCMV infection are negligible.

In summary, our data reveal that the canonical function of IRE1 is required for optimal proliferation of virus-specific NK cells, but that lack of cell-intrinsic IRE1 in NK cells does not hamper organismal viral control.

DISCUSSION

Like virus-specific B and T cells, innate immune system NK cells expand dramatically upon MCMV infection, with some adoptive transfer experiments showing up to 1000-fold expansion of Ly49H^{+} NK cells within a few days.[9] To keep up with this high proliferation rate, NK cells must undergo profound rewiring of their metabolic programs and recent studies highlighted the need of both aerobic glycolysis and oxidative

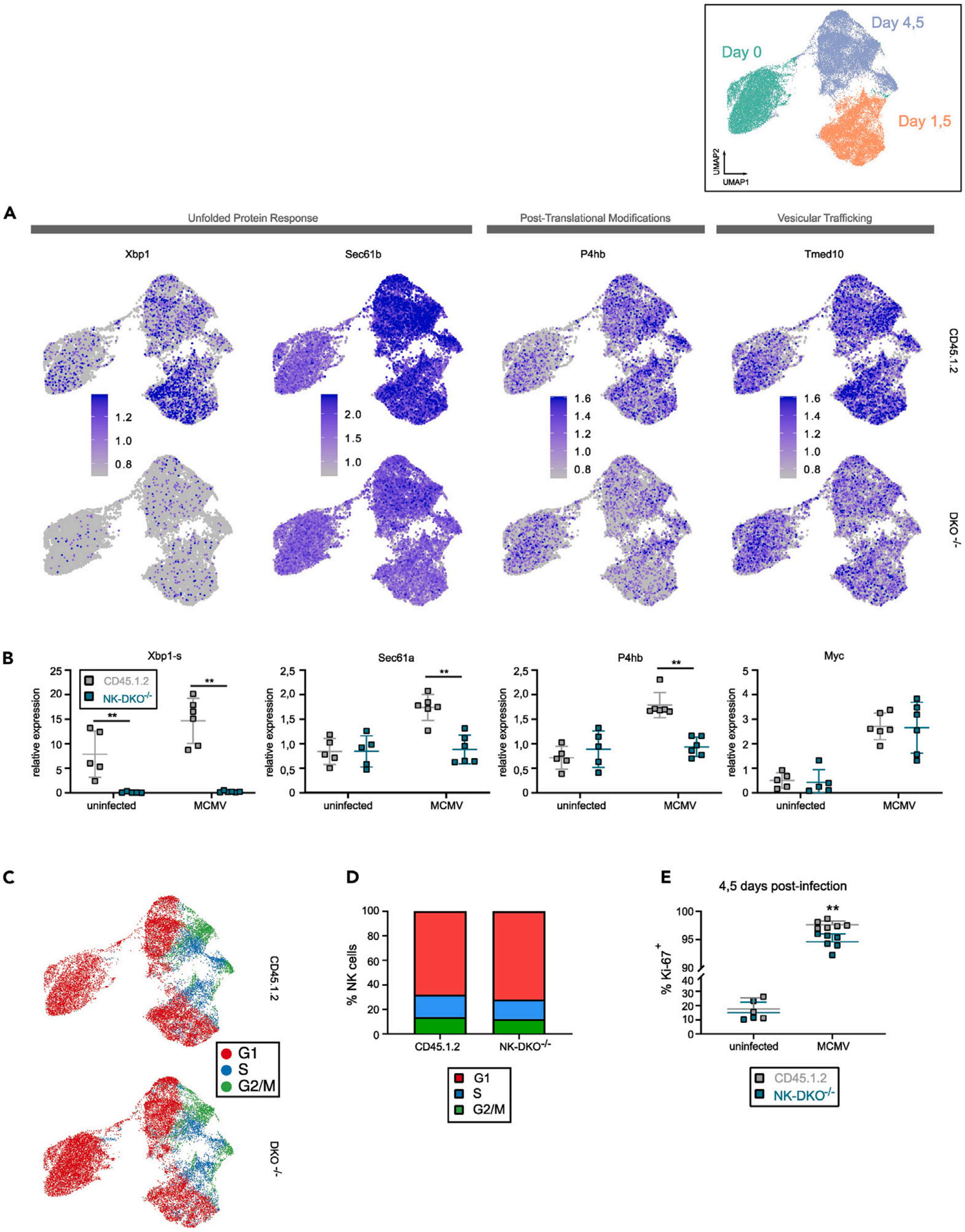

Figure 7. Loss of IRE1/XBP1 impairs virus-mediated activation of the unfolded protein response

(A) UMAP feature plots, split by genotype (WT and DKO$^{-/-}$), showing the expression of representative genes belonging to the most relevant enriched GO categories. The cells on the plot are ordered according to expression, resulting in cells with high expression being plotted on top. The color scale represents normalized gene and surface expression.

(B) qPCR on RNA isolated from CD45.1.2 and CD45.2 DKO$^{-/-}$sorted splenic NK cells of mixed bone marrow chimeras at days 0 or 1,5 post-MCMV. Bar graphs represent expressions of Myc, Xbp1-s, Sec61a and P4hb as normalized to Hprt and Ywhaz.

(C) UMAP of cell cycle stages, split by genotype (WT and DKO$^{-/-}$). The color codes highlight the different cell cycle stages.

(D) Stacked bar plot of WT and DKO $^{-/-}$ NK cells over the three cell cycle phases.

(E) Bar graphs display the percentage of Ki-67^{+} NK cells among the total Ly49H^{+} population at days 0 or 4,5 post-infection. All experiments were performed once, with the exception of (E) displaying representative data from 1 out of 2 independent experiments. Bar graphs depict mean ± SD and individual mice are represented by dots. See also Figure S5 and Tables S2, S6–S8. Mann-Whitney U test was performed on data in panel B and E with $^{*}p < 0.05$; $^{**}p < 0.01$; $^{***}p < 0.001$; $^{****}p < 0.0001$.

phosphorylation to sustain viral-induced proliferation and to control MCMV infection.[53] In addition, several metabolic regulators such as mTOR and c-myc are well known mediators of NK cell homeostasis and function, both in steady state and during viral infection or cytokine-mediated activation of NK cells.[54–56] How upstream environmental cues connect to these metabolic pathways is not always well-understood.

It was previously reported that MCMV infection triggers early and transient activation of the IRE1 signaling branch, without activation of PERK and ATF6,[18] an observation that we here confirmed. IRE1 does not seem to be important for the development or homeostasis of NK cells, and neither bulk RNA-Seq nor CITE-Seq revealed major differences in gene expression profiles between WT and IRE1/XBP1-deficient NK cells in steady state. At first sight, also the NK cell-mediated response to viral infection appeared largely unaffected in absence of IRE1/XBP1. Early activation markers such as CD69 were similarly expressed, IFNγ production and cytotoxic properties of NK cells were unimpaired, and viral loads were equal between WT and DKO$^{-/-}$ animals undergoing MCMV infection. Still, competitive settings such as adoptive transfer experiments or competitive mixed bone marrow chimeras revealed that IRE1/XBP1-proficient NK cells had a clear advantage compared to IRE1/XBP1-deficient ones and almost completely outcompeted them over the time course of the experiment. In agreement with earlier observations,[18] our data indicated that loss of IRE1 led to a defect in virus-induced NK cell expansion in a competitive setting. To understand how loss of IRE1 affected the transcriptional response to viral infection, hence might interfere with virus-induced NK cell expansion, we applied CITE-Seq technology, a method in which single cell RNA-Seq is combined with cell surface epitope sequencing by using a library of more than 150 barcoded antibodies.

Unexpectedly, this revealed that WT and IRE1/XBP1-deficient NK cells largely activated the same gene programs upon MCMV infection as Louvain clustering and UMAP dimensionality reduction showed no difference between WT and DKO$^{-/-}$ NK cells. Recently, IRE1 was proposed as a key regulator of c-myc activation in conditions of MCMV infection in NK cells.[18] However, we could not attribute the defect in virus-induced NK cell expansion to a defect in *c-myc* signaling or in activation of cell cycle genes as none of these programs appeared differentially expressed upon loss of IRE1/XBP1, an observation in line with earlier data.[19] At this point, it is not entirely clear where the discrepancy with the previous study comes from,[18] although it underscores the difficulty of interpreting bulk RNA-Seq data when comparing populations that might differ in composition. We know that in mixed bone marrow chimeras, already early upon infection, WT cells have a competitive advantage and proliferate more rapidly than their DKO$^{-/-}$ counterparts[18,] this study. In this respect, it might be no surprise that cell cycle genes or proliferation-regulating genes such as *c-myc* might turn up as being DE genes when performing bulk RNA-Seq. This does not necessarily imply that they are direct target genes of the IRE1/XBP1 branch but could just reflect differences in cellular composition. In conditions where the numbers of WT and DKO$^{-/-}$ cells were equally matched, we could not retrieve any differences in the amount of WT or DKO$^{-/-}$ cells in the G1, S and G2/M phases, showing that the DKO$^{-/-}$ NK cells do not suffer from any intrinsic defect in proliferation. This is also supported by our observations that IRE1/XBP1-deficient NK cells do expand in response to viral infection, although even in a non-competitive setting there was always a slightly reduced amount of Ly49H$^+$ NK cells compared to WT cells.

Therefore, we believe that this study supports the canonical role of the UPR in endowing the ER with a fully operational folding machinery, needed for NK cells (and likely any other immune cell type) to quickly respond to environmental cues such as viral infection and sustain vigorous proliferation. This would lead to a competitive advantage for cells with a proficient folding response and optimal metabolic fitness. Due to the clonal expansion of NK cells in response to MCMV, this has a major effect on the cellular outcome on the long term of WT versus IRE1/XBP1-deficient cells in competitive settings. Overall, however, the IRE1 pathway is largely dispensable for NK cell development, homeostasis and their ability to control viral infections.

Limitations of the study

The major caveat of this study comprises the absence of a direct link between IRE1 deficiency and observed defects in NK cell expansion during viral infection. While our data indicate that a general decrease in cellular fitness due to loss of an important branch of the UPR negatively affects NK cell proliferation upon MCMV infection, further research is warranted to unravel the underlying molecular mechanism in more detail.

STAR★METHODS

Detailed methods are provided in the online version of this paper and include the following:

- KEY RESOURCES TABLE
- RESOURCE AVAILABILITY
  - Lead contact
  - Materials availability
  - Data and code availability
- EXPERIMENTAL MODEL AND STUDY PARTICIPANT DETAILS
  - *In vivo* animal studies
  - Virus
- METHOD DETAILS
  - Bone marrow chimeras and adoptive cell transfers
  - *In vivo* treatments

- ○ *In vivo* virus infection
- ○ Virus quantification
- ○ Single cell suspensions
- ○ Flow cytometry and fluorescence-activated cell sorting
- ○ *Ex vivo* stimulations and labeling
- ○ ELISA
- ○ RNA extraction, conventional PCR and qPCR
- ○ Bulk RNA sequencing
- ○ CITE-Sequencing
- ● QUANTIFICATION AND STATISTICAL ANALYSIS

SUPPLEMENTAL INFORMATION

Supplemental information can be found online at https://doi.org/10.1016/j.isci.2023.108570.

ACKNOWLEDGMENTS

We thank the members of the Janssens lab for helpful discussions of the experimental data and comments on the manuscript. We thank the labs of Vivier and Gasteiger for providing virus and essential mouse strains used in this study. We also thank all involved VIB core facilities such as the Animal House, Cell Culture and Singularity for their continuous support and logistics. We would like to thank the VIB Flow Core for training, support and access to the instrument park.

The research was funded by an ERC Consolidator Grant (DCRIDDLE- 819314), FWO program grants (G017521N and G063218N), a BOF research grant from the University of Ghent (BOF24Y2017000601) and EOS grant (G0G7318N).

AUTHOR CONTRIBUTIONS

Conceptualization, J.V., M.v.H., B.N.L., and S.J.; Methodology, J.V., M.V.H., B.N.L., and S.J.; Investigation, J.V., S.R., E.C., E.V.D.V., F.F., J.V.M., M.V., and K.V.; Formal analysis, J.V. and C.D.N.; Data curation, C.D.N.; Visualization, J.V. and C.D.N.; Resources, E.V. and L.B.; Writing – Original draft, J.V. and S.J.; Writing – Review and Editing, J.V. and S.J.; Supervision, M.v.H. and S.J.

DECLARATION OF INTERESTS

E.V. is a cofounder and employee of Innate Pharma. All other authors declare no competing interests.

Received: August 25, 2023
Revised: October 16, 2023
Accepted: November 21, 2023
Published: November 23, 2023

REFERENCES

1. Spits, H., Bernink, J.H., and Lanier, L. (2016). NK cells and type 1 innate lymphoid cells: partners in host defense. Nat. Immunol. *17*, 758–764.
2. Mujal, A.M., Delconte, R.B., and Sun, J.C. (2021). Natural Killer Cells: From Innate to Adaptive Features. Annu. Rev. Immunol. *39*, 417–447.
3. Sun, J.C., and Lanier, L.L. (2011). NK cell development, homeostasis and function: parallels with CD8$^+$ T cells. Nat. Rev. Immunol. *11*, 645–657.
4. Vivier, E., Tomasello, E., Baratin, M., Walzer, T., and Ugolini, S. (2008). Functions of natural killer cells. Nat. Immunol. *9*, 503–510.
5. Lanier, L.L. (2008). Up on the tightrope: natural killer cell activation and inhibition. Nat. Immunol. *9*, 495–502.
6. Adams, N.M., Geary, C.D., Santosa, E.K., Lumaquin, D., Le Luduec, J.B., Sottile, R., van der Ploeg, K., Hsu, J., Whitlock, B.M., Jackson, B.T., et al. (2019). Cytomegalovirus Infection Drives Avidity Selection of Natural Killer Cells. Immunity *50*, 1381–1390.e5.
7. Grassmann, S., Pachmayr, L.O., Leube, J., Mihatsch, L., Andrae, I., Flommersfeld, S., Oduro, J., Cicin-Sain, L., Schiemann, M., Flossdorf, M., and Buchholz, V.R. (2019). Distinct Surface Expression of Activating Receptor Ly49H Drives Differential Expansion of NK Cell Clones upon Murine Cytomegalovirus Infection. Immunity *50*, 1391–1400.e4.
8. Dokun, A.O., Kim, S., Smith, H.R., Kang, H.S., Chu, D.T., and Yokoyama, W.M. (2001). Specific and nonspecific NK cell activation during virus infection. Nat. Immunol. *2*, 951–956.
9. Sun, J.C., Beilke, J.N., and Lanier, L.L. (2009). Adaptive immune features of natural killer cells. Nature *457*, 557–561.
10. Hetz, C., and Papa, F.R. (2018). The Unfolded Protein Response and Cell Fate Control. Mol. Cell *69*, 169–181.
11. Tabas, I., and Ron, D. (2011). Integrating the mechanisms of apoptosis induced by endoplasmic reticulum stress. Nat. Cell Biol. *13*, 184–190.
12. Walter, P., and Ron, D. (2011). The unfolded protein response: from stress pathway to homeostatic regulation. Science *334*, 1081–1086.
13. Lee, A.H., Iwakoshi, N.N., and Glimcher, L.H. (2003). XBP-1 regulates a subset of endoplasmic reticulum resident chaperone genes in the unfolded protein response. Mol. Cell Biol. *23*, 7448–7459.
14. Yoshida, H., Matsui, T., Yamamoto, A., Okada, T., and Mori, K. (2001). XBP1 mRNA is induced by ATF6 and spliced by IRE1 in response to ER stress to produce a highly active transcription factor. Cell *107*, 881–891.
15. Hollien, J., and Weissman, J.S. (2006). Decay of endoplasmic reticulum-localized mRNAs during the unfolded protein response. Science *313*, 104–107.
16. Grootjans, J., Kaser, A., Kaufman, R.J., and Blumberg, R.S. (2016). The unfolded protein response in immunity and inflammation. Nat. Rev. Immunol. *16*, 469–484.
17. Janssens, S., Pulendran, B., and Lambrecht, B.N. (2014). Emerging functions of the unfolded protein response in immunity. Nat. Immunol. *15*, 910–919.
18. Dong, H., Adams, N.M., Xu, Y., Cao, J., Allan, D.S.J., Carlyle, J.R., Chen, X., Sun, J.C., and Glimcher, L.H. (2019). The IRE1 endoplasmic reticulum stress sensor activates natural killer

cell immunity in part by regulating c-Myc. Nat. Immunol. *20*, 865–878.

19. Ma, S., Han, J., Li, Z., Xiao, S., Zhang, J., Yan, J., Tang, T., Barr, T., Kraft, A.S., Caligiuri, M.A., and Yu, J. (2023). An XBP1s-PIM-2 positive feedback loop controls IL-15-mediated survival of natural killer cells. Sci. Immunol. *8*, eabn7993.
20. Ydens, E., Amann, L., Asselbergh, B., Scott, C.L., Martens, L., Sichien, D., Mossad, O., Blank, T., De Prijck, S., Low, D., et al. (2020). Profiling peripheral nerve macrophages reveals two macrophage subsets with distinct localization, transcriptome and response to injury. Nat. Neurosci. *23*, 676–689.
21. Osorio, F., Tavernier, S.J., Hoffmann, E., Saeys, Y., Martens, L., Vetters, J., Delrue, I., De Rycke, R., Parthoens, E., Pouliot, P., et al. (2014). The unfolded-protein-response sensor IRE-1α regulates the function of CD8α+ dendritic cells. Nat. Immunol. *15*, 248–257.
22. Tavernier, S.J., Lambrecht, B.N., and Janssens, S. (2018). The Unfolded Protein Response in the Immune Cell Development: Putting the Caretaker in the Driving Seat. Curr. Top. Microbiol. Immunol. *414*, 45–72.
23. Iwawaki, T., Akai, R., Kohno, K., and Miura, M. (2004). A transgenic mouse model for monitoring endoplasmic reticulum stress. Nat. Med. *10*, 98–102.
24. Narni-Mancinelli, E., Chaix, J., Fenis, A., Kerdiles, Y.M., Yessaad, N., Reynders, A., Gregoire, C., Luche, H., Ugolini, S., Tomasello, E., et al. (2011). Fate mapping analysis of lymphoid cells expressing the NKp46 cell surface receptor. Proc. Natl. Acad. Sci. USA *108*, 18324–18329.
25. Caton, M.L., Smith-Raska, M.R., and Reizis, B. (2007). Notch-RBP-J signaling controls the homeostasis of CD8- dendritic cells in the spleen. J. Exp. Med. *204*, 1653–1664.
26. Iwawaki, T., Akai, R., Yamanaka, S., and Kohno, K. (2009). Function of IRE1 alpha in the placenta is essential for placental development and embryonic viability. Proc. Natl. Acad. Sci. USA *106*, 16657–16662.
27. Chiossone, L., Chaix, J., Fuseri, N., Roth, C., Vivier, E., and Walzer, T. (2009). Maturation of mouse NK cells is a 4-stage developmental program. Blood *113*, 5488–5496.
28. Hayakawa, Y., and Smyth, M.J. (2006). CD27 dissects mature NK cells into two subsets with distinct responsiveness and migratory capacity. J. Immunol. *176*, 1517–1524.
29. Kim, S., Iizuka, K., Kang, H.S.P., Dokun, A., French, A.R., Greco, S., and Yokoyama, W.M. (2002). In vivo developmental stages in murine natural killer cell maturation. Nat. Immunol. *3*, 523–528.
30. Alter, G., Malenfant, J.M., and Altfeld, M. (2004). CD107a as a functional marker for the identification of natural killer cell activity. J. Immunol. Methods *294*, 15–22.
31. Martinon, F., Chen, X., Lee, A.H., and Glimcher, L.H. (2010). TLR activation of the transcription factor XBP1 regulates innate immune responses in macrophages. Nat. Immunol. *11*, 411–418.
32. Bensellam, M., Chan, J.Y., Lee, K., Joglekar, M.V., Hardikar, A.A., Loudovaris, T., Thomas, H.E., Jonas, J.C., and Laybutt, D.R. (2019). Phlda3 regulates beta cell survival during stress. Sci. Rep. *9*, 12827.
33. Han, C.Y., Lim, S.W., Koo, J.H., Kim, W., and Kim, S.G. (2016). PHLDA3 overexpression in hepatocytes by endoplasmic reticulum stress via IRE1-Xbp1s pathway expedites liver injury. Gut *65*, 1377–1388.
34. Bouton, M.C., Boulaftali, Y., Richard, B., Arocas, V., Michel, J.B., and Jandrot-Perrus, M. (2012). Emerging role of serpinE2/protease nexin-1 in hemostasis and vascular biology. Blood *119*, 2452–2457.
35. Heraud-Farlow, J.E., and Kiebler, M.A. (2014). The multifunctional Staufen proteins: conserved roles from neurogenesis to synaptic plasticity. Trends Neurosci. *37*, 470–479.
36. Thakur, H.C., Singh, M., Nagel-Steger, L., Prumbaum, D., Fansa, E.K., Gremer, L., Ezzahoini, H., Abts, A., Schmitt, L., Raunser, S., et al. (2013). Role of centrosomal adaptor proteins of the TACC family in the regulation of microtubule dynamics during mitotic cell division. Biol. Chem. *394*, 1411–1423.
37. Biron, C.A., Byron, K.S., and Sullivan, J.L. (1989). Severe herpesvirus infections in an adolescent without natural killer cells. N. Engl. J. Med. *320*, 1731–1735.
38. Mace, E.M., and Orange, J.S. (2019). Emerging insights into human health and NK cell biology from the study of NK cell deficiencies. Immunol. Rev. *287*, 202–225.
39. Fodil-Cornu, N., Lee, S.H., Belanger, S., Makrigiannis, A.P., Biron, C.A., Buller, R.M., and Vidal, S.M. (2008). Ly49h-deficient C57BL/6 mice: a new mouse cytomegalovirus-susceptible model remains resistant to unrelated pathogens controlled by the NK gene complex. J. Immunol. *181*, 6394–6405.
40. Stoeckius, M., Hafemeister, C., Stephenson, W., Houck-Loomis, B., Chattopadhyay, P.K., Swerdlow, H., Satija, R., and Smibert, P. (2017). Simultaneous epitope and transcriptome measurement in single cells. Nat. Methods *14*, 865–868.
41. Flommersfeld, S., Böttcher, J.P., Ersching, J., Flossdorf, M., Meiser, P., Pachmayr, L.O., Leube, J., Hensel, I., Jarosch, S., Zhang, Q., et al. (2021). Fate mapping of single NK cells identifies a type 1 innate lymphoid-like lineage that bridges innate and adaptive recognition of viral infection. Immunity *54*, 2288–2304.e7.
42. Crinier, A., Milpied, P., Escalière, B., Piperoglou, C., Galluso, J., Balsamo, A., Spinelli, L., Cervera-Marzal, I., Ebbo, M., Girard-Madoux, M., et al. (2018). High-Dimensional Single-Cell Analysis Identifies Organ-Specific Signatures and Conserved NK Cell Subsets in Humans and Mice. Immunity *49*, 971–986.e5.
43. McFarland, A.P., Yalin, A., Wang, S.Y., Cortez, V.S., Landsberger, T., Sudan, R., Peng, V., Miller, H.L., Ricci, B., David, E., et al. (2021). Multi-tissue single-cell analysis deconstructs the complex programs of mouse natural killer and type 1 innate lymphoid cells in tissues and circulation. Immunity *54*, 1320–1337.e4.
44. van Helden, M.J., Goossens, S., Daussy, C., Mathieu, A.L., Faure, F., Marçais, A., Vandamme, N., Farla, N., Mayol, K., Viel, S., et al. (2015). Terminal NK cell maturation is controlled by concerted actions of T-bet and Zeb2 and is essential for melanoma rejection. J. Exp. Med. *212*, 2015–2025.
45. Rahim, M.M.A., Tu, M.M., Mahmoud, A.B., Wight, A., Abou-Samra, E., Lima, P.D.A., and Makrigiannis, A.P. (2014). Ly49 receptors: innate and adaptive immune paradigms. Front. Immunol. *5*, 145.
46. Adams, N.M., Lau, C.M., Fan, X., Rapp, M., Geary, C.D., Weizman, O.E., Diaz-Salazar, C., and Sun, J.C. (2018). Transcription Factor IRF8 Orchestrates the Adaptive Natural Killer Cell Response. Immunity *48*, 1172–1182.e6.
47. Bezman, N.A., Kim, C.C., Sun, J.C., Min-Oo, G., Hendricks, D.W., Kamimura, Y., Best, J.A., Goldrath, A.W., and Lanier, L.L.; Immunological Genome Project Consortium (2012). Molecular definition of the identity and activation of natural killer cells. Nat. Immunol. *13*, 1000–1009.
48. Fogel, L.A., Sun, M.M., Geurs, T.L., Carayannopoulos, L.N., and French, A.R. (2013). Markers of nonselective and specific NK cell activation. J. Immunol. *190*, 6269–6276.
49. Leavenworth, J.W., Verbinnen, B., Wang, Q., Shen, E., and Cantor, H. (2015). Intracellular osteopontin regulates homeostasis and function of natural killer cells. Proc. Natl. Acad. Sci. USA *112*, 494–499.
50. Lucas, T.M., Richner, J.M., and Diamond, M.S. (2015). The Interferon-Stimulated Gene Ifi27l2a Restricts West Nile Virus Infection and Pathogenesis in a Cell-Type- and Region-Specific Manner. J. Virol. *90*, 2600–2615.
51. Zhao, X., Li, J., Winkler, C.A., An, P., and Guo, J.T. (2018). IFITM Genes, Variants, and Their Roles in the Control and Pathogenesis of Viral Infections. Front. Microbiol. *9*, 3228.
52. Kowalczyk, M.S., Tirosh, I., Heckl, D., Rao, T.N., Dixit, A., Haas, B.J., Schneider, R.K., Wagers, A.J., Ebert, B.L., and Regev, A. (2015). Single-cell RNA-seq reveals changes in cell cycle and differentiation programs upon aging of hematopoietic stem cells. Genome Res. *25*, 1860–1872.
53. Mah-Som, A.Y., Keppel, M.P., Tobin, J.M., Kolicheski, A., Saucier, N., Sexl, V., French, A.R., Wagner, J.A., Fehniger, T.A., and Cooper, M.A. (2021). Reliance on Cox10 and oxidative metabolism for antigen-specific NK cell expansion. Cell Rep. *35*, 109209.
54. Vetters, J., van Helden, M.J., Wahlen, S., Tavernier, S.J., Martens, A., Fayazpour, F., Vergote, K., Vanheerswynghels, M., Deswarte, K., Van Moorleghem, J., et al. (2019). The ubiquitin-editing enzyme A20 controls NK cell homeostasis through regulation of mTOR activity and TNF. J. Exp. Med. *216*, 2010–2023.
55. Viel, S., Marçais, A., Guimaraes, F.S.F., Loftus, R., Rabilloud, J., Grau, M., Degouve, S., Djebali, S., Sanlaville, A., Charrier, E., et al. (2016). TGF-β inhibits the activation and functions of NK cells by repressing the mTOR pathway. Sci. Signal. *9*, ra19.
56. Loftus, R.M., Assmann, N., Kedia-Mehta, N., O'Brien, K.L., Garcia, A., Gillespie, C., Hukelmann, J.L., Oefner, P.J., Lamond, A.I., Gardiner, C.M., et al. (2018). Amino acid-dependent cMyc expression is essential for NK cell metabolic and functional responses in mice. Nat. Commun. *9*, 2341.
57. Kamimura, Y., and Lanier, L.L. (2014). Rapid and sequential quantitation of salivary gland-associated mouse cytomegalovirus in oral lavage. J. Virol. Methods *205*, 53–56.
58. Bolger, A.M., Lohse, M., and Usadel, B. (2014). Trimmomatic: a flexible trimmer for Illuminasequence data. Bioinformatics *30*, 2114–2120.
59. Dobin, A., Davis, C.A., Schlesinger, F., Drenkow, J., Zaleski, C., Jha, S., Batut, P., Chaisson, M., and Gingeras, T.R. (2013). STAR: ultrafast universal RNA-seq aligner. Bioinformatics *29*, 15–21.
60. Danecek, P., Bonfield, J.K., Liddle, J., Marshall, J., Ohan, V., Pollard, M.O., Whitwham, A., Keane, T., McCarthy, S.A., Davies, R.M., and Li, H. (2021). Twelve years of SAMtools and BCFtools. GigaScience *10*, giab008.

61. Anders, S., Pyl, P.T., and Huber, W. (2015). HTSeq–a Python framework to work with high-throughput sequencing data. Bioinformatics *31*, 166–169.
62. Ritchie, M.E., Phipson, B., Wu, D., Hu, Y., Law, C.W., Shi, W., and Smyth, G.K. (2015). limma powers differential expression analyses for RNA-sequencing and microarray studies. Nucleic Acids Res. *43*, e47.
63. Robinson, M.D., McCarthy, D.J., and Smyth, G.K. (2010). edgeR: a Bioconductor package for differential expression analysis of digital gene expression data. Bioinformatics *26*, 139–140.
64. Satija, R., Farrell, J.A., Gennert, D., Schier, A.F., and Regev, A. (2015). Spatial reconstruction of single-cell gene expression data. Nat. Biotechnol. *33*, 495–502.
65. McCarthy, D.J., Campbell, K.R., Lun, A.T.L., and Wills, Q.F. (2017). Scater: pre-processing, quality control, normalization and visualization of single-cell RNA-seq data in R. Bioinformatics *33*, 1179–1186.
66. Lun, A.T.L., McCarthy, D.J., and Marioni, J.C. (2016). A step-by-step workflow for low-level analysis of single-cell RNA-seq data with Bioconductor. F1000Res. *5*, 2122.
67. McGinnis, C.S., Murrow, L.M., and Gartner, Z.J. (2019). DoubletFinder: Doublet Detection in Single-Cell RNA Sequencing Data Using Artificial Nearest Neighbors. Cell Syst. *8*, 329–337.e4.
68. Crowell, H.L., Soneson, C., Germain, P.L., Calini, D., Collin, L., Raposo, C., Malhotra, D., and Robinson, M.D. (2020). muscat detects subpopulation-specific state transitions from multi-sample multi-condition single-cell transcriptomics data. Nat. Commun. *11*, 6077.
69. Love, M.I., Huber, W., and Anders, S. (2014). Moderated estimation of fold change and dispersion for RNA-seq data with DESeq2. Genome Biol. *15*, 550.
70. Yu, G., Wang, L.-G., Han, Y., and He, Q.-Y. (2012). clusterProfiler: an R package for comparing biological themes among gene clusters. OMICS *16*, 284–287.
71. Smedley, D., Haider, S., Ballester, B., Holland, R., London, D., Thorisson, G., and Kasprzyk, A. (2009). BioMart - biological queries made easy. BMC Genom. *10*, 22.
72. Edgar, R., Domrachev, M., and Lash, A.E. (2002). Gene Expression Omnibus: NCBI gene expression and hybridization array data repository. Nucleic Acids Res. *30*, 207–210.
73. Weizman, O.E., Adams, N.M., Schuster, I.S., Krishna, C., Pritykin, Y., Lau, C., Degli-Esposti, M.A., Leslie, C.S., Sun, J.C., and O'Sullivan, T.E. (2017). ILC1 Confer Early Host Protection at Initial Sites of Viral Infection. Cell *171*, 795–808.e12.

STAR★METHODS

KEY RESOURCES TABLE

REAGENT or RESOURCE	SOURCE	IDENTIFIER
Antibodies		
Rat anti-mouse CD3 (clone 17A2), PerCP-eFluor710 conjugated	Thermo Fisher Scientific	Cat# 46-0032-82; RRID:AB_1834427
Rat anti-mouse CD3 (clone 17A2), eFluor450 conjugated	Thermo Fisher Scientific	Cat# 48-0032-82; RRID:AB_1272193
Armenian hamster anti-mouse CD3e (clone 145-2c11), PE-Cy5 conjugated	Thermo Fisher Scientific	Cat# 15-0031-83; RRID:AB_468691
Armenian hamster anti-mouse CD3e (clone 145-2c11), PE-Cy7 conjugated	BioLegend	Cat# 100320; RRID:AB_312685
Armenian Hamster anti-mouse CD3e (clone 145-2c11), biotin conjugated	Thermo Fisher Scientific	Cat# 13-0031-85; RRID:AB_466320
Rat anti-mouse CD11b (clone M1/70), V450 conjugated	BD Biosciences	Cat# 560455; RRID:AB_1645266
Rat anti-mouse CD11b (clone M1/70), APC-eFluor780 conjugated	Thermo Fisher Scientific	Cat# 47-0112-82; RRID:AB_1603193
Rat anti-mouse CD11b (clone M1/70), PE conjugated	BD Biosciences	Cat# 553311; RRID:
Hamster anti-mouse CD11c (clone N418), eFluor450 conjugated	Life Technologies Europe BV	Cat# 48-0114-82; RRID:AB_1548654
Armenian Hamster anti-mouse CD11c (clone N418), APC conjugated	BioLegend	Cat# 117310; RRID:AB_313778
Armenian hamster anti-mouse CD11c (clone N418), PE-Cy7 conjugated	Thermo Fisher Scientific	Cat# 25-0114-82; RRID:AB_469590
Rat anti-mouse CD19 (clone 1D3), APC conjugated	BD Biosciences	Cat# 550992; RRID:AB_398483
Rat anti-mouse CD19 (clone eBio1D3), AF700 conjugated	Thermo Fisher Scientific	Cat# 56-0193-82; RRID:AB_837083
Rat anti-mouse CD19 (clone eBio1D3), PE-Cy5 conjugated	Thermo Fisher Scientific	Cat# 15-0193-83; RRID:AB_657673
Rat anti-mouse CD19 (clone 1D3), PE-Cy7 conjugated	Life Technologies Europe BV	Cat# 25-0193-82; RRID:AB_657663
Rat anti-mouse CD19 (clone 1D3), biotin conjugated	Thermo Fisher Scientific	Cat# 13-0193-85; RRID:AB_657658
Armenian Hamster anti-mouse CD27 (clone LG.7F9), PE-Cy7 conjugated	Thermo Fisher Scientific	Cat# 25-0271-82; RRID:AB_1724035
Rat anti-mouse CD45 (clone 30-F11), BV605 conjugated	BD Biosciences	Cat# 563053; RRID:AB_2737976
Rat anti-mouse CD45 (clone 30-F11), APC-eFluor780 conjugated	Thermo Fisher Scientific	Cat# 47-0451-82; RRID:AB_1548781
Mouse anti-mouse CD45.1 (clone A20), BV605 conjugated	BioLegend	Cat# 110738; RRID:AB_2562565
Mouse anti-mouse CD45.2 (clone 104), PerCP-Cy5.5 conjugated	BD Biosciences	Cat# 552950; RRID:AB_394528
Rat anti-mouse CD49b (clone DX5), FITC conjugated	Thermo Fisher Scientific	Cat# 11-5971-82; RRID:AB_465327

(*Continued on next page*)

Continued

REAGENT or RESOURCE	SOURCE	IDENTIFIER
Rat anti-mouse CD49b (clone DX5), eFluor450 conjugated	Life Technologies Europe BV	Cat# 48-5971-82; RRID:AB_10671541
Mouse anti-mouse CD64 (clone X54-5/7.1), BV421 conjugated	BioLegend	Cat# 139309; RRID:AB_2562694
Armenian hamster anti-mouse CD69 (clone H1.21F3), PerCP-Cy5.5 conjugated	BD Biosciences	Cat# 551113; RRID:AB_394051
Armenian hamster anti-mouse CD69 (clone H1.21F3), PE-Cy7 conjugated	BD Biosciences	Cat# 561930; RRID:AB_10893591
Rat anti-mouse CD107 (clone 1DB4), PE conjugated	BD Biosciences	Cat# 558661; RRID:AB_1645247
Rat anti-mouse CD122 (clone TM-b1), PerCP-eFluor710 conjugated	Life Technologies Europe BV	Cat# 46-1222-82; RRID:AB_11064442
Mouse anti-mouse CD161 (PK136), unconjugated	Life Technologies Europe BV	Cat# 16-5941-85; RRID:AB_469160
Mouse anti-mouse CD161 (clone PK136), BV605 conjugated	BioLegend	Cat# 108740; RRID:AB_2562273
Mouse anti-mouse CD161 (clone PK136), APC conjugated	BD Biosciences	Cat# 550627; RRID:AB_398463
Mouse anti-mouse CD161 (clone PK136), PE conjugated	BD Biosciences	Cat# 553165; RRID:AB_394677
Rat anti-mouse CD172a (clone P84), PE-Cy7 conjugated	BioLegend	Cat# 144008; RRID:AB_2563546
Armenian hamster anti-mouse CD314 (clone A10), unconjugated	Life Technologies Europe BV	Cat# 16-5872-82; RRID:AB_469107
Rat anti-mouse CD335 (clone 29A1.4), APC conjugated	BioLegend	Cat# 137608; RRID:AB_10612749
Rat anti-mouse CD335 (clone 29A1.4), eFluor450 conjugated	BioLegend	Cat# 48-3351-82; RRID:AB_10557245
Rat anti-mouse F4/80 (clone BM8), BV786 conjugated	BioLegend	Cat# 123141; RRID:AB_2563667
Rat anti-mouse I-A/I-E (clone M5/114.15.2), PerCP-Cy5.5 conjugated	BioLegend	Cat# 107626; RRID:AB_2191072
Rat anti-mouse I-A/I-E (clone M5/114.15.2), APC-eFluor780 conjugated	Thermo Fisher Scientific	Cat# 47-5321-82; RRID:AB_1548783
Rat anti-mouse IFNγ (clone XMG1.2), eFluor450 conjugated	Thermo Fisher Scientific	Cat# 48-7311-82; RRID:AB_1834366
Mouse anti-mouse Ki-67 (clone B56), BV786 conjugated	BD Biosciences	Cat# 563756; RRID:AB_2732007
Golden syrian hamster anti-mouse KLRG1 (clone 2F1), APC conjugated	Life Technologies Europe BV	Cat# 17-5893-82; RRID:AB_469469
Rat anti-mouse Ly-6G (clone 1A8), biotin conjugated	BioLegend	Cat# 127604; RRID:AB_1186105
Rat anti-mouse Ly49D (clone 400000), unconjugated	BioLegend	Cat# 138302; RRID:AB_10574460
Rat anti-mouse Ly49D (clone 400000), PE conjugated	Miltenyi Biotec	Cat #130-102-416; RRID:AB_2652712
Mouse anti-mouse Ly49H (clone 3D10), APC conjugated	Life Technologies Europe BV	Cat# 17-5886-82; RRID:AB_10598809
Mouse anti-mouse Ly49H (clone 3D10), PE-Cy7 conjugated	BioLegend	Cat# 144714; RRID:AB_2783112

(*Continued on next page*)

Continued

REAGENT or RESOURCE	SOURCE	IDENTIFIER
Armenian hamster anti-mouse TCRβ (clone H57-597), APC-eFluor780 conjugated	BioLegend	Cat# 109220; RRID:AB_893624
Armenian hamster anti-mouse TCRβ (clone H57-597), biotin conjugated	Life Technologies Europe BV	Cat# 13-5961-82; RRID:AB_466819
Rat anti-mouse TER-119 (clone TER-119), biotin conjugated	Thermo Fisher Scientific	Cat# 13-5921-82; RRID:AB_466797
Mouse anti-mouse XCR1 (clone ZET), PE conjugated	BioLegend	Cat# 148204; RRID:AB_2563843
Rat anti-mouse anti-CD16/CD32 (clone 2.4G2), unconjugated (Fc block)	Bioceros	N/A
Bacterial and virus strains		
MCMV Smith Strain	Eric Vivier lab, CIML, FR	N/A
Chemicals, peptides, and recombinant proteins		
2-Mercaptoethanol	Sigma	Cat# M3148
2-Mercaptoethanol	Cell Culture Core VIB	N/A
5-ethynyl-2′-deoxyuridine (EdU)	Thermo Fisher Scientific	Cat# E10187
Annexin V, PE conjugated	BD Biosciences	Cat# 556422
Annexin V Binding Buffer	BD Biosciences	Cat# 556422
Bovine Serum Albumin (BSA)	Sigma	Cat@ A7030
Buffer RLT Plus	Qiagen	Cat # 1053393
Cell Proliferation Dye eFluor450	Thermo Fisher Scientific	Cat# 65-0842-90
Collagenase A	Roche	Cat# 11088793001
DNAse I recombinant, Grade I	Roche	Cat# 04536282001
EDTA	Westburg	Cat# 51234
Fetal calf serum (FCS)	Bodinco	N/A
Fetal calf serum (FCS)	Greiner	N/A
Fixable viability dye Live/Dead eFluor506	Thermo Fisher Scientific	Cat# 65-0866-18
Fixable viability dye Live/Dead eFluor780	Thermo Fisher Scientific	Cat# 65-0865-14
Gentamicin	Gibco	
GlutaMAX Supplement	Thermo Fisher Scientific	Cat# 35050038
GolgiStop Protein Transport Inhibitor	BD biosciences	Cat# 554724
Liberase TM Research Grade	Roche	Cat# 05401127001
Percoll	GE Healthcare	Cat# 17-0891-01
Poly(I:C)	Invivogen	Cat# tlrl-pic
Recombinant Murine IL-2	PeproTech	Cat# 212-12
Recombinant Murine IL-12 p70	PeproTech	Cat# 210-12
Recombinant Murine IL-15	PeproTech	Cat# 210-15
Recombinant IL-18	Tebu-Bio NV	Cat# RPA064Mu01
TriPure Isolation Reagent	Roche	Cat # 11667165001
Critical commercial assays		
Click-iT Plus EdU Alexa Fluor 647 Flow cytometry assay kit	Thermo Fisher Scientific	Cat# C10634
Cytofix/Cytoperm Fixation/Permeabilization Kit	BD Biosciences	Cat# 554714
DNeasy Mini Blood & Tissue Kit	Qiagen	Cat# 69504
Foxp3/Transcription Factor Staining Buffer Set	Thermo Fisher Scientific	Cat# 00-5523-00

(*Continued on next page*)

Continued

REAGENT or RESOURCE	SOURCE	IDENTIFIER
GoTaq G2 Green Master Mix 2X	Promega	Cat# M7823
IFN gamma Mouse ELISA Kit	Thermo Fisher Scientific	Cat# 88-7314-77
MagniSort Mouse NK cell Enrichment Kit	Thermo Fisher Scientific	Cat# 8804-6828-74
MinElute Reaction Cleanup Kit	Qiagen	Cat# 28204
Ovation PicoSL WTA System V2 Kit	Tecan	Cat# 3312-48
RNEasy Plus Micro Kit	Qiagen	Cat# 74034
SensiFAST cDNA Synthesis Kit	Bioline	Cat# BIO - 65054
SensiFAST SYBR No-ROX Kit	Bioline	Cat# BIO-98020
Deposited data		
Bulk RNA-Seq splenic NK cells	This paper	GSE236822
CITE-Seq splenic NK cells	This paper	GSE236822
Experimental models: Organisms/strains		
Mouse: BALB/cJ	Charles River	N/A
Mouse: B6.SJL-Ptprc^{a} Pepc^{b}/BoyJ	The Jackson Laboratory; maintained through in-house breeding	RRID: IMSR_JAX:002014
Mouse: B6.SJL-Ptprc^{a} Pepc^{b}/BoyJ.Ptprc^{b}	In-house breeding	N/A
Mouse: B6.TG$^{pCAX\text{-}F\text{-}XBP\text{-}1DBD\text{-}venus}$/J	In-house breeding	N/A
Mouse: B6.Klra8$^{Cmv1\text{-}del}$ .SJL-Ptprc^{a} Pepc^{b}/BoyJ	Klra8^{Cmv1del} mice: Georg Gasteiger lab, Würzburg, DE. Further in-house breeding to obtain this line	N/A
Mouse: B6.Xbp1^{tm2Glm}-Ncr1$^{tm1.1(icre)Viv}$/J	Ncr1^{iCre} mice: Eric Vivier lab, CIML, FR. Further in-house breeding to obtain this line	N/A
Mouse: B6.Ern1^{tm1Tiw} .Xbp1 ^{tm2Glm} -Ncr1$^{tm1.1(icre)Viv}$/J	Ncr1^{iCre} mice: Vivier lab, CIML, FR. Further in-house breeding to obtain this specific line	N/A
Oligonucleotides		
Actin-beta F: 5′-GTGACGTTGACATCCGTAAAGA-3′	IDT	N/A
Actin-beta R: 5′-GCCGGACTCATCGTACTCC-3′	IDT	N/A
Birc5 F: 5′-GAGGCTGGCTTCATCCACTG-3′	IDT	N/A
Birc5 R:5′-ATGCTCCTCTATCGGGTTGTC-3′	IDT	N/A
Cdk4 F: 5′-ATGGCTGCCACTCGATATGAA-3′	IDT	N/A
Cdk4 R: 5′-TCCTCCATTAGGAACTCTCACAC-3′	IDT	N/A
Cdkn1a F: 5′-CGAGAACGGTGGAACTTTGAC-3′	IDT	N/A
Cdkn1a R: 5′-CCAGGGCTCAGGTAGACCTT-3′	IDT	N/A
Ddx18 F: 5′-CCTCGCTTTCCTCATCCCTG-3′	IDT	N/A
Ddx18 R: 5′-TGAACGTGGTGCGTCATCAG-3′	IDT	N/A
Ern1 F: 5′-TGCTGAAACACCCCTTCTTC-3′	IDT	N/A
Ern1 R: 5′-GCCTCCTTTTCTATTCGGTCA-3′	IDT	N/A
Gapdh F: 5′-GCATGGCCTTCCGTGTTC-3′	IDT	N/A
Gapdh R: 5′-TGTCATCATACTTGGCAGGTTTCT-3′	IDT	N/A
Hprt F: 5′-TGAAGAGCTACTGTAATGATCAGTCAAC-3′	IDT	N/A
Hprt R: 5′-AGCAAGCTTGCAACCTTAACCA-3′	IDT	N/A
Ki-67 F: 5′-ATCATTGACCGCTCCTTTAGGT-3′	IDT	N/A
Ki-67 R: 5′- GCTCGCCTTGATGGTTCCT-3′	IDT	N/A
Myc F: 5′-ATGCCCCTCAACGTGAACTTC-3′	IDT	N/A

(*Continued on next page*)

Continued

REAGENT or RESOURCE	SOURCE	IDENTIFIER
Myc R: 5′-GTCGCAGATGAAATAGGGCTG-3′	IDT	N/A
MCMV-IE1 F: 5′-TCGCCCATCGTTTCGAGA-3′	IDT	N/A
MCMV-IE1 R: 5′-TCTCGTAGGTCCACTGACCGA -3′	IDT	N/A
P4hb F: 5′-CAAGATCAAGCCCCACCTGAT-3′	IDT	N/A
P4hb R: 5′-AGTTCGCCCCAACCAGTACTT-3′	IDT	N/A
Pim-2 F: 5′-TTCAGCGGGCTCAATATACGC-3′	IDT	N/A
Pim-2 R: 5′-CCAAGTCGGTATTCGGCCTC -3′	IDT	N/A
Rrm2 F: 5′-TGGCTGACAAGGAGAACACG-3′	IDT	N/A
Rrm2 R: 5′- AGGCGCTTTACTTTCCAGCTC -3′	IDT	N/A
Sec61a F: 5′-CTGGCGGTAGAATGCCTCT-3′	IDT	N/A
Sec61a R: 5′-TGAGACCATTGTGTGGAAGG-3′	IDT	N/A
Tbp F: 5′-TCTACCGTGAATCTTGGCTGTAAA-3′	IDT	N/A
Tbp R: 5′-TTCTCATGATGACTGCAGCAAA-3′	IDT	N/A
Top2a F: 5′-CAACTGGAACATATACTGCTCCG -3′	IDT	N/A
Top2a R: 5′-GGGTCCCTTTGTTTGTTATCAGC –3′	IDT	N/A
Xbp1 exon 2 F: 5′-CAGCAAGTGGTGGATTTGG-3′	IDT	N/A
Xbp1 exon 2 R: 5′-CGTGAGTTTTCTCCCGTAAAAG-3′	IDT	N/A
Xbp1 (u+s) F: 5′-ACACGCTTGGGAATGGACAC-3′	IDT	N/A
Xbp1 (u+s) R: 5′-CCATGGGAAGATGTTCTGGG-3′	IDT	N/A
Xbp1-s F: 5′-TGCTGAGTCCGCAGCAGGTG-3′	IDT	N/A
Xbp1-s R: 5′-ACTTGTCCAGAATGCCCAAAAGGA-3′	IDT	N/A
Ywhaz F: 5′-CTCTTGGCAGCTAATGGGCTT-3′	IDT	N/A
Ywhaz R: 5′-GGAGGTGGCTGAGGATGGA-3′	IDT	N/A
Recombinant DNA		
MCMV-IE1 plasmid	Kamimura and Lanier.[57]	N/A
Software and algorithms		
BD FACSDiva v8.0.2	BD Biosciences	RRID: SCR_001456
FlowJo v10.7	FlowJo LLC	www.flowjo.com; RRID: SCR_008520
GraphPad Prism 9	GraphPas Software	www.flowjo.com; RRID: SCR_008520
qBase+ v3.2	CellCarta	qbaseplus.com; RRID:SCR_003370
Cell Ranger v6.0.0	10x Genomics	RRID: SCR_017344
R Project for Statistical Computing v3.6.1	www.r-project.org	RRID: SCR_001905
R Studio v1.2.1335	https://www.rstudio.com/	RRID: SCR_000432
Trimmomatic v0.39	Bolger et al.[58]	RRID: SCR_011848
FastQC v0.11.8	https://www.bioinformatics.babraham.ac.uk/projects/fastqc/	RRID: SCR_014583
STAR v2.7.3a	Dobin et al.[59]	RRID: SCR_004463
Samtools v1.9	Danecek et al.[60]	RRID: SCR_002105
HTSeqCount v0.11.2	Anders et al.[61]	RRID: SCR_011867
Limma v3.42.2	Ritchie et al.[62]	RRID: SCR_010943
EdgeR v3.28.1	Robinson et al.[63]	RRID: SCR_012802
pheatmap v1.0.12	https://CRAN.R-project.org/package=pheatmap	RRID: SCR_016418

(*Continued on next page*)

Continued

REAGENT or RESOURCE	SOURCE	IDENTIFIER
Seurat v3.1.4	Satija et al.[64]	RRID: SCR_016341
Scater v1.14.6	McCarthy et al.[65]	RRID: SCR_015954
Scran v1.14.6	Lun et al.[66]	RRID: SCR_016944
DoubletFinder v2.0.2	McGinnis et al.[67]	RRID: SCR_018771
Muscat v1.1.0	Crowell et al.[68]	https://github.com/HelenaLC/muscat
DESeq2 v1.26.0	Love et al.[69]	RRID: SCR_015687
ClusterProfiler v3.14.3	Yu et al.[70]	RRID: SCR_016884
BiomaRt v2.42.1	Smedley et al.[71]	RRID: SCR_002987
Other		
DMEM	Gibco	Cat# 41965-039
RPMI 1640	Gibco	Cat# 52400-025

RESOURCE AVAILABILITY

Lead contact

Further information and requests for resources and reagents should be directed to and will be fulfilled by the lead contact, Prof. dr. Sophie Janssens (sophie.janssens@irc.vib-ugent.be).

Materials availability

This study did not generate new unique reagents.

Data and code availability

- All raw sequencing data enclosed in this publication has been deposited in NCBI's Gene Expression Omnibus[72] and is accessible through GEO Series accession number GSE236822 (https://www.ncbi.nlm.nih.gov/geo/query/acc.cgi?acc=GSE236822). All single-cell datasets provided in this manuscript can be accessed in an online tool via the following link: https://www.single-cell.be/splenic-NK-profiles-MCMV.
- This paper does not report original code.
- Any additional information required to reanalyze the data reported in this paper is available from the lead contact upon request.

EXPERIMENTAL MODEL AND STUDY PARTICIPANT DETAILS

In vivo animal studies

All mice used in this study were housed and bred under specific pathogen-free conditions at the VIB Center for Inflammation Research. BALB/c mice were ordered from Charles River. All animal experiments were performed in accordance with institutional guidelines for animal care of the VIB site Ghent-Ghent University Faculty of Sciences and in accordance with ethical committees EC2017-029, EC2021-067 and EC2023-99. Mouse lines used in this study were: *Ncr1*$^{iCre/+}$,[24] *Xbp1*$^{fl/fl}$,[25] *Ire1*$^{fl/fl}$ x *Xbp1*$^{fl/fl}$,[26] Ly49H$^{-/-}$ ([39]; a kind gift from Georg Gasteiger), CD45.1 and CD45.1.2. The Ly49H$^{-/-}$ line was crossed onto the CD45.1 line and all mouse lines were generated on a C57Bl/6J background. For steady state experiments, mice from both genders (6-12 weeks) were used. MCMV experiments were limited to male mice (8-14 weeks), with the exception of virus production in female BALB/c mice (3 weeks). For bone marrow chimera experiments animals were euthanized at 20-60 weeks.

Virus

MCMV Smith strain was serially passaged in BALB/c animals once more upon arrival of the P2 virus batch, a kind gift from the Vivier lab. Animal's salivary glands were collected two weeks later and viral stocks were prepared by Dounce homogenation in DMEM (Gibco) supplemented with 3% FCS (Bodinco). Aliquots were stored at minus 80°C.

METHOD DETAILS

Bone marrow chimeras and adoptive cell transfers

Bone marrow chimeras: CD45.1 recipient animals were sublethally irradiated with 2 rounds of 400cG, with respect of a 4 hour interval in between two irradiations. At least 4 hours after the second irradiation cycle, recipient mice received an intravenous injection with a 50:50 mixture of bone marrow cells (3-4x10^6 cells in total) derived from CD45.1.2 and NK-DKO$^{+/+}$ or NK-DKO$^{-/-}$ animals. Mice were used at least 8 weeks later after establishing successful reconstitution. Adoptive cell transfers: NK cells were isolated and enriched from the spleens of CD45.1.2, NK-DKO$^{+/+}$ and NK-DKO$^{-/-}$ animals. 50:50 mixtures containing equal numbers of sort-purified Ly49H$^+$ NK cells (2x10^5 cells total) from CD45.1.2 and NK-DKO$^{+/+}$ or NK-DKO$^{-/-}$ origin were administered intravenously (iv) into Ly49H$^{-/-}$ recipients.

In vivo treatments

For EdU labeling experiments, mice received a single ip injection of 2 mg EdU (Thermo Fisher Scientific) in PBS 12 hours prior to sacrifice at indicated time points post-MCMV. ERAi mice received a single ip injection with 100 μg poly(I:C) (Invivogen) in PBS for 12 hours.

In vivo virus infection

Mice were infected with MCMV by intraperitoneal (ip) injection of 2,5x10^4 or 5x10^4 pfu/g (administered in DMEM (Gibco)) in case of mild viral infections or survival studies, respectively. For adoptive cell transfers, Ly49H$^{-/-}$ recipients received 7,5x10^3 pfu/g MCMV ip one day later than receiving an iv injection containing the 50:50 cell mixture of choice. Mixed bone marrow chimeras were infected with 2x10^4 pfu/g MCMV by ip injection.

Virus quantification

MCMV viral titers were determined as previously described.[73] In short, DNA was isolated from peripheral blood of infected animals with the DNeasy Mini Blood & Tissue Kit (Qiagen) per manufacturer's instructions. DNA concentration was measured with Nanodrop and 3 μl purified viral DNA was used as input for SensiFAST sybr no ROX (Bioline) quantitative polymerase chain reaction (qPCR). Primers for MCMV immediate early 1 (IE1) were as follows: 5′-TCGCCCATCGTTTCGAGA-3′ (forward) and 5′-TCTCGTAGGTCCACTGACCGA-3′ (reverse). Viral loads were determined by comparing Cq values to a standard curve generated by serially diluting the MCMV IE1 plasmid[57] with a known concentration. Viral loads are shown on total DNA content per sample.

Single cell suspensions

Spleens were either subjected to an enzymatic digestion protocol (Figures 1A and 1B) or smashed over a 70 μm filter to subsequently remove all red blood cells by osmotic lysis. In the former case, spleens were minced and then digested for 30 minutes in RPMI 1640 (Gibco) containing Liberase TM (0,02 mg/ml; Roche) and DNase I (10U/ml; Roche) in a shaking water bath at 37°C, including resuspension after 15 minutes. Next, cell suspensions were filtered over a 70 μm filter, followed by osmotic lysis for red blood cell removal. For bone marrow, single cell suspensions were obtained by crushing the tibia and femur of a single hind leg, followed by lysis of red blood cells. In the case of lung and liver, organs were first perfused with PBS before organ isolation. Lungs were minced and digested at 37°C for 30 minutes in RPMI 1640 (Gibco) containing DNase I (10 U/ml; Roche) and collagenase A (2,4 mg/ml; Sigma), including resuspension after 15 minutes. GentleMACS dissociation (prior to and after digestion) was required for the lungs and red blood cells were removed by osmotic lysis. Livers were smashed over a 70 μm filter, followed by 37,5% Percoll-gradient centrifugation and red blood cell lysis. Blood was drawn from the tail vein or by a. femoralis (terminal) bleeding and collected in eppendorfs pre-coated with 50-100 μl 0,5M EDTA (Lonza), respectively. Red blood cells were cleared by two rounds of osmotic lysis.

Flow cytometry and fluorescence-activated cell sorting

Upon preparation of single cell suspensions, 3-5x10^6 cells or an enriched fraction (see further) were stained with one or more fluorochrome- or biotin-linked monoclonal antibodies targeting the following markers: CD3, CD11b, CD11c, CD19, CD27, CD45, CD45.1, CD45.2, CD49b, CD64, CD69, CD107, CD122, CD161, CD172a, CD314, CD335, F4/80, I-A/I-E, IFNγ, Ki-67, KLRG1, Ly49D, Ly49H, Ly6G, TCRβ, Ter119, XCR1. Cells were treated with Fc block (2.4G2, Bioceros) to limit aspecific binding and live cells were distinguished by use of fixable viability dyes (eBioscience) and/or annexinV staining (BD Biosciences) per manufacturer's instructions to determine NK cell survival. Intracellular stainings for Ki-67 were performed with the Foxp3 kit (eBioscience), while Cytofix/Cytoperm and Perm/Wash (both from BD) were used for intracellular IFNγ measurements. EdU labeling was determined with the Click-iT EdU Assay Kit (Thermo Fisher Scientific). Flow cytometry was performed on a FACS Fortessa 4 or 5 laser or FACSymphony A5 (all from BD Biosciences). Gating strategy for flow was as follows: B cells (CD3$^-$CD19$^+$IA-IE$^+$), cDC1s (CD3$^-$CD19$^-$NK1.1$^-$CD11c$^+$IA-IE$^+$XCR1$^+$), cDC2s (CD3$^-$CD19$^-$NK1.1$^-$,CD11c$^+$IA-IE$^+$XCR1$^-$CD11b$^+$), NK cells (CD3$^-$CD19$^-$NK1.1$^+$NKp46$^+$CD122$^+$CD49b$^+$), T cells (CD3$^+$CD19$^-$). Of note, the applied cDC2 gating strategy does not include markers to fully exclude macrophage contamination. In case of fluorescence-activated cell sorting, obtained splenic single cell suspensions were enriched prior to sorting. Enrichment was performed with the MagniSort NK cell enrichment kit (eBioscience) or with an in-house optimized biotinylated antibody enrichment cocktail (against CD3, CD19, Ly6G, TCRβ and Ter119), followed by magnetic separation of cells by negative selection. For experiments requiring simultaneous sorting of lymphocyte populations and DCs, the obtained single cell suspensions were divided in two fractions: one fraction (approx. 5x10^6 cells) was immediately stained for T and B cells, the other fraction was enriched for NK cells and DCs prior to staining. Sorting was performed on a FACS Aria II or III or a FACSymphony A6 cell sorter (all from BD Biosciences). Upon sorting, cells were collected in appropriate recipients pre-coated with PBS supplemented with 5mM EDTA and 1% BSA or PBS supplemented with 0,5% BSA only. After washing, cells were either loaded for CITE-Seq or pellets were either resuspended in Tripure or RLT Plus Buffer (RNEasy plus micro kit, Qiagen) supplemented with 2-mercaptoethanol (10 μl/ml). In the latter two cases, samples were snap frozen and stored at minus 80°C until further processing. The following gating strategies were applied: B cells (CD3$^-$CD19$^+$), cDC1s

(CD3$^-$CD19$^-$NK1.1$^-$CD64$^-$F4/80$^-$CD11c$^+$IA-IE$^+$XCR1$^+$), cDC2s (CD3$^-$CD19$^-$NK1.1$^-$CD64$^-$F4/80$^-$CD11c$^+$IA-IE$^+$CD172a$^+$), NK cells (CD3$^-$CD19$^-$TCRβ$^-$NK1.1$^+$NKp46$^+$CD49b$^+$) and T cells (CD19-NK1.1$^-$CD3$^+$).

Ex vivo stimulations and labeling

In adoptive transfer setups, total splenocytes were labeled with 0,5 μM CellTrace Violet (eBioscience) during a 10 min incubation at 37 degrees. CTV was quenched by a three-fold washing step in a FCS-supplemented PBS-based buffer. For IFNγ/CD107a functional studies, 3x10^6 splenocytes were cultured in RPMI 1640 (Gibco) supplemented with 10% FCS (Greiner) in the presence of GolgiStop (BD) and anti-CD107a (BD). Cells were cultured in MaxiSorp flat-bottom plates (Nunc) for 4 hours at 37°C after overnight pre-coating with antibodies (anti-NK1.1 and anti-Ly49D at 10 μg/ml, anti-NKG2D at 5μg/ml) or in presence of cytokine stimulation (rmIL-12 at 25 ng/ml, rmIL-18 at 5 ng/ml and rmIL-2 at 20 ng/ml (all from Peprotech)). For ELISA, 2x10^4 sort-purified splenic NK cells, isolated from either uninfected or 1,5 days MCMV infected animals, were cultured in tissue culture medium containing RPMI 1640 (Gibco), 10% FCS (Greiner), Glutamax (LifeTechnologies), Gentamicin (Gibco) and β-mercaptoethanol (Cell Culture Core, VIB). Tissue culture medium was supplemented with a low dose of rmIL-15 (10 ng/ml, Peprotech) in presence or absence of cytokine stimulation (rmIL-12 at 25 ng/ml and rmIL-18 at 5 ng/ml, both from Peprotech). After 24 hours, plates were spun down, culture supernatant was collected and stored at minus 20°C.

ELISA

IFNγ ELISA (eBioscience) was performed in accordance to manufacturer's guidelines on culture supernatant obtained from *ex vivo* stimulations.

RNA extraction, conventional PCR and qPCR

RNA was isolated from sort-purified immune cell populations with the TriPure Isolation Reagent (Sigma) or RNEasy Plus Micro Kit (Qiagen). While the former method was used for qPCRs concerning mouse model validation (Figure 1; Figure S1), the latter method was used for CITE-Seq validation qPCRs (Figure 7) or conventional PCR and bulk RNA-Seq. For conventional PCR, nanodrop was used to determine RNA concentrations and normalize RNA input across samples. cDNA was generated with the SensiFAST cDNA Synthesis Kit (Bioline) according to manufacturer's instructions, followed by conventional PCR with GoTaq G2 Green Master Mix 2X (Promega) or by qPCR with the SensiFast SYBR No-ROX kit (Bioline). For Figure 7 qPCRs, RNA quality was checked by Agilent 2100 BioAnalyzer, amplified with Ovation PicoSL WTA system V2 (Nugen) and cleaned up with the MinElute Reaction Cleanup Kit (Qiagen) per manufacturer's instructions. Conventional PCR was performed on a thermal cycler (BioRad) and bands were separated by height with gel electrophoresis; qPCR was performed on a LightCycler 480 (Roche). The following mouse primers were used (first two pairs for conventional PCR, the remaining pairs for qPCR): XBP1 (u+s) F: 5′-ACACGCTTGGGAATGGACAC-3′; XBP1 (u+s) R: 5′-CCATGGGAAGATGTTCTGGG-3′; Actin-beta F: 5′-GTGACGTTGACATCCGTAAAGA-3′; Actin-beta R: 5′-GCCGGACTCATCGTACTCC-3′; Birc5 F: 5′-GAGGCTGGCTTCATCCACTG-3′; Birc5 R:5′-ATGCTCCTCTATCGGGTTGTC-3′; Cdk4 F: 5′-ATGGCTGCCACTCGATATGAA-3′; Cdk4 R: 5′-TCCTCCATTAGGAACTCTCACAC-3′; Cdkn1a F: 5′-CGAGAACGGTGGAACTTTGAC-3′; Cdkn1a R: 5′-CCAGGGCTCAGGTAGACCTT-3′; Ddx18 F: 5′- CCTCGCTTTCCTCATCCCTG -3′; Ddx18 R: 5′-TGAACGTGGTGCGTCATCAG-3′; Ern1 F: 5′-TGCTGAAACACCCCTTCTTC-3′; Ern1 R: 5′-GCCTCCTTTTCTATTCGGTCA-3′; Gapdh F: 5′-GCATGGCCTTCCGTGTTC-3′; Gapdh R: 5′-TGTCATCATACTTGGCAGGTTTCT-3′; Hprt F: 5′-TGAAGAGCTACTGTAATGATCAGTCAAC-3′; Hprt R: 5′-AGCAAGCTTGCAACCTTAACCA-3′; Ki-67 F: 5′-ATCATTGACCGCTCCTTTAGGT-3′; Ki-67 R: 5′-GCTCGCCTTGATGGTTCCT-3′; MCMV-IE1 F: 5′-TCGCCCATCGTTTCGAGA-3′; MCMV-IE1 R: 5′-TCTCGTAGGTCCACTGACCGA -3′; Myc F: 5′-ATGCCCCTCAACGTGAACTTC-3′; Myc R: 5′-GTCGCAGATGAAATAGGGCTG-3′; P4hb F: 5′-CAAGATCAAGCCCCACCTGAT-3′; P4hb R: 5′-AGTTCGCCCCAACCAGTACTT-3′; Pim-2 F: 5′-TTCAGCGGGCTCAATATACGC-3′; Pim-2 R: 5′- CCAAGTCGGTATTCGGCCTC-3′; Rrm2 F: 5′-TGGCTGACAAGGAGAACACG-3′; Rrm2 R: 5′- AGGCGCTTTACTTTCCAGCTC-3′; Sec61a F: 5′-CTGGCGGTAGAATGCCTCT-3′; Sec61a R: 5′-TGAGACCATTGTGTGGAAGG-3′; Sdha F: 5′-TTTCAGAGACGGCCATGATCT-3′; Sdha R: 5′-TGGGAATCCCACCCATGTT-3′; Tbp F: 5′-TCTACCGTGAATCTTGGCTGTAAA-3′; TbpR: 5′-TTCTCATGATGACTGCAGCAAA-3′; Top2a F: 5′- CAACTGGAACATATACTGCTCCG-3′; Top2a R: 5′-GGGTCCCTTTGTTTGTTATCAGC-3′; Xbp1 exon 2 F: 5′-CAGCAAGTGGTGGATTTGG-3′; Xbp1 exon 2 R: 5′-CGTGAGTTTTCTCCCGTAAAAG-3′; Xbp1-s F: 5′-TGCTGAGTCCGCAGCAGGTG-3′; Xbp1-s R: 5′-ACTTGTCCAGAATGCCCAAAAGGA-3′; Ywhaz F: 5′-CTCTTGGCAGCTAATGGGCTT-3′; Ywhaz R: 5′-GGAGGTGGCTGAGGATGGA-3′.

Bulk RNA sequencing

RNA integrity was assessed using a Bioanalyzer 2100 (Agilent). Sequencing was carried out by VIB Nucleomics Core (www.nucleomics.be) on an Illumina HiSeq 4000 instrument. Preprocessing of the RNA-Seq data was performed by Trimmomatic v0.39 and quality control by FastQC v0.11.8. Mapping to the reference mouse genome was accomplished by STAR v2.7.3a, BAM files were created with Samtools v1.9 and HTSeqCount v0.11.2 was used for counting. Limma v3.42.2 was used to normalize the data. Genes which did not meet the requirement of a count per million (cpm) value larger than 1 in at least 4 samples were filtered. This resulted in an expression table containing 10906 genes for the splenic NK cell dataset in steady state. EdgeR v3.28.1 was utilized to perform differential expression analysis. The R package pheatmap v1.0.12 was used to create a heatmap of all the DE genes between the three conditions (NK-XBP1-KO, NK-DKO and WT) in splenic NK cells. The displayed gene expression was log2 normalized. The mean expression value per gene over all replicates was calculated and then subtracted from each replicate's particular gene expression value to scale the expression values.

CITE-Sequencing

Sorting and library prep

NK cells were enriched as previously described and approx. 4x10^{6} cells were stained with flow antibodies, TruStain FcX Block (BioLegend, 101320) and the mouse cell surface protein antibody panel containing 165 oligo-conjugated antibodies (TotalSeq-A, BioLegend) and 9 TotalSeq-A isotype controls (Table S2). Based on treatment and day of the infection, the following number of NK cells (gated as: live, CD3^{-}CD19^{-}TCRβ^{-}NK1.1^{+}CD49b^{+}) and lymphocytes (gated as: live, non-NK) were sorted: 1,9x10^{5} uninfected, 6-6,5x10^{4} at 1,5 dpi and 7-8x10^{4} at 4,5 dpi. We respectively used n=2, n=4 or n=10 mixed bone marrow chimeras for days 0, 1,5 and 4,5 post-infection and hashing antibodies were used to label the separate biological replicates at each timepoint. This strategy enabled us to apply robust statistics in the downstream analysis while limiting sequencing costs. On day 1,5 samples were pooled 2 by 2 post-sorting, while on day 4,5 samples were pooled during sorting (to avoid losing cells in the additional steps as cell numbers were already on the low side). Of note, one of the biological replicates (with hashtag 3) had to be removed from the analysis as it did not respond to the given MCMV infection. Sorted single-cell suspensions were resuspended at an estimated final concentration of 1000 cells/μl and loaded on a Chromium GemCode Single Cell Instrument (10x Genomics) to generate single-cell gel beads-in-emulsion (GEM). The scRNA-Seq libraries were prepared using the GemCode Single Cell 3′ Gel Bead and Library kit, version NextGEM 3.1 (10x Genomics) according to the manufacturer's instructions with the addition of amplification primer (3 nM, 5′CCTTGGCACCCGAGAATT*C*C) during cDNA amplification to enrich the TotalSeq-A cell surface protein oligos. Size selection with SPRIselect Reagent Kit (Beckman Coulter) was used to separate amplified cDNA molecules for 3′ gene expression and cell surface protein construction. TotalSeq-A protein library construction including sample index PCR using Illumina's Truseq Small RNA primer sets and SPRIselect size selection was performed according to the manufacturer's instructions. The cDNA content of pre-fragmentation and post-sample index PCR samples was analyzed using the 2100 BioAnalyzer (Agilent).

CITE-Seq analysis

Sequencing libraries were loaded on an Illumina NovaSeq flow cell at VIB Nucleomics core with sequencing settings according to the recommendations of 10x Genomics, pooled in a 70:20:10 ratio for the combined 3′ gene expression, cell surface protein samples and HashTag-Oligo (HTO) data, respectively. The Cell Ranger pipeline (10x Genomics, v6.0.0) was used to perform sample demultiplexing and to generate FASTQ files for read 1 and read 2 for the gene expression and cell surface protein libraries. Read 2 of the gene expression libraries was mapped to the reference genome (mouse mm10) using STAR. Subsequent barcode processing, unique molecular identifiers filtering and gene counting was performed using the Cell Ranger suite. CITE-Seq reads were quantified using the feature-barcoding functionality. The mean reads per cell across all expression libraries were 27499 RNA reads and 2515 ADT reads respectively, with an average sequencing saturation of 56,4% and 66%, as calculated by Cell Ranger. 6 individual single-cell libraries were analyzed for this experiment, totaling 76,918 cells. After individual analysis, the resulting Seurat objects were merged into a WT object and a DKO object. These objects were further investigated, subsequently subsetted to only NK cells and finally merged into a complete object.

Pre-processing data

Pre-processing of the RNA UMI matrix of each sample was done by the scater and scran R packages (v1.14.6) according to the workflow proposed by the Marioni lab.[66] Outlier cells were identified based on three metrics (library size, number of expressed genes and mitochondrial proportion) and an initial lenient filtering was performed on these outlier cells according to median absolute deviation (MADs). Log-transformed normalized expression values were then computed from the count matrix. Subsequently the Seurat R package (v3.1.4) was used to create a Seurat object for each sample with both the raw counts and log2 transformed counts. SCTransform was performed on the raw count data to normalize the UMI counts by regularized negative binomial regression. Additionally, highly variable features were found and scaling was performed on the log-transformed count data as a back-up for SCT. Principal component analysis, clustering and tSNE/UMAP dimensionality reduction were performed. DoubletFinder (v2.0.2) was performed to predict any remaining doublets in the dataset. The ADT UMI matrix did not have extensive pre-processing performed. The same cells were filtered as during the RNA pre-processing to keep the columns of the matrices equal. The ADT expression data was processed using the Seurat pipeline, with CLR normalization and scaling of the data performed using the default parameters. Principal component analysis, clustering and tSNE/UMAP dimensionality reduction were performed too. Marker genes per identified subpopulation were found using the findMarkers function of the Seurat pipeline and this informed the annotation process of the clusters. The HTO assay was transformed via CLR normalization. Biological replicates in each sample were demultiplexed by running the MULTIseqDemux function included in Seurat. It is based on the classification method from MULTI-seq. The autoTresh parameter of the probability density function (PDF) was set to True. After annotating all individual samples, the WT samples were merged into a WT object and the DKO samples into a DKO object. Subsequently for each object, an NK cell subset was created and the same Seurat pipeline was performed as above. The DoubletFinder and MULTI-Seq annotation together with ADT metrics and information on mitochondrial proportion, UMI count and gene count was used to filter doublets, contaminating cells and low-quality clusters. One replicate (denoted with HTO3) had to be removed from the analysis as the MCMV infection appeared unsuccessful. This was confirmed by biological data (lack of weight loss). Lastly, the NK cell subsets of WT and DKO samples were merged into a complete NK cell subset object and the same Seurat pipeline was performed as above.

Differential state analysis

The comparison between DKO and WT NK cells was performed using the R package muscat (v1.1.0). It allows for Differential State (DS) analysis in multi-sample, multi-group, multi-(cell-)subpopulation scRNA-Seq data. The RNA data for the two genotypes was aggregated for total NK cells at day 1,5 and day 4,5, respectively, and a "pseudobulk" DS analysis was performed between the two genotypes. The DS analysis utilized the DESeq2 method. The DS results were filtered according to local adjusted p-value and logFC to retain the biologically significant results. Overview cluster-sample average expression heatmaps with the top 50 significant downregulated DE genes at day 1,5 and day 4,5, respectively, were created with Seurat to visualize the top results.

Functional annotation

Gene ontology (GO) enrichment analysis was performed using the clusterProfiler R package v3.14.3. To study MCMV progression in WT NK cells, this was carried out on the DE gene sets attained by running the FindMarker function from Seurat between all WT NK cells of each timepoint respectively. Conversely, to study the difference between the genotypes during MCMV infection, this was conducted on the DE gene sets of the muscat DS analysis at day 1,5 and day 4,5 respectively. Only "Biological Pathway" GO terms were included in the enrichment analysis. The top 30 significantly enriched BP GO categories are featured in the dot plots for the prior analysis, while for the latter analysis, only the top 10 significantly enriched BP GO categories are featured. The top GO categories in each dot plot are ordered according to geneRatio which is the ratio of the input DE gene set annotated in the respective GO term. The adjusted p-value is displayed as the color of the dot and the size of the dot is determined by the Count parameter, which is the number of DE genes annotated in the respective GO term.

CellCycleScoring Seurat

All WT and DKO$^{-/-}$ NK cells were split up into phases by calculating cell cycle phase scores based on canonical markers, from.[52] The list consists of markers of the G2/M phase and the S phase and is loaded with Seurat. The human gene names were converted to mouse gene names by using the biomaRt package (v2.42.1). The scores from the CellCycleScoring function were stored in the seurat object meta data. Based on these scores, cells could be assigned to either the G1, S or G2M phase.

Cell cycle phase WT/DKO$^{-/-}$ NK cell stacked bar plot

NK cells were split by genotype and cell cycle phase into six groups and the resulting cell count of each group was divided by the total NK cell count of their respective genotype to calculate percentages. This was performed to take into account the difference in total population size between the genotypes. This percentage data was then used to generate a stacked bar plot of WT and DKO$^{-/-}$ NK cells over the three cell cycle phases.

QUANTIFICATION AND STATISTICAL ANALYSIS

Data sets were analyzed with one of the following three statistical tests: Mann-Whitney U, Kruskal-Wallis combined with Dunn's multiple comparisons or Mantel-Cox. All statistical tests were performed with the Prism/GraphPad Software. P-values express the levels of significance (*, $P<0,05$; **, $P<0,01$; ***, $P<0,001$; ****, $P<0,0001$) and error bars represent the standard deviation. For RNA-Seq, EdgeR v3.28.1 was utilized to perform differential expression analysis. Benjamini-Hochberg correction was used to adjust the p-values for multiple testing. To be labelled as a DE gene, a gene needed to have an adjusted p-value smaller than 0.05 and a log2-ratio > 1 or < - 1. For CITE-Seq, differential expression analysis to determine the cluster markers was performed using the Wilcoxon Rank Sum test through the Seurat functions FindAllMarkers and FindMarkers. P-value adjustment was accomplished with Bonferroni correction. RNA and ADT markers for the annotated clusters were determined with these cutoffs: min.pct = 0,10, logfc.threshold = 0,25 and return.thresh (adj. P-value) = 0,01. Only positive markers were evaluated. An extra "score" column was calculated as a way to rank the importance of the genes as markers. It was calculated with this function: "pct.1/(pct.2+0,01)*avg_logFC". The markers are ordered according to this score. Differential State analysis to determine the differential markers for total NK cells between DKO and WT at day 1,5 and day 4,5 was performed using DESeq2 within muscat. P-value adjustment was performed using Benjamini-Hochberg correction at a local level (per cluster). Significant differentially expressed (DE) genes were determined by using these cut-offs: p_adj.loc < 0,05 and |logFC| > 0,25. Functional annotation was performed with clusterProfiler v3.14.3. P-value adjustment was achieved with the Benjamini-Hochberg procedure, an adjusted p-value cut-off of 0,05 was utilized to determine the significantly enriched GO terms.